Near-storm Environmental Relationships with Tropical Oceanic Convective Structure Observed during NASA CPEX and CPEX-AW

Benjamin D. Rodenkirch

A Thesis submitted in partial fulfillment of
the requirements for the degree of
Master of Science
(Atmospheric and Oceanic Sciences)

at the
University of Wisconsin-Madison
2023

Graduate School
UNIVERSITY OF WISCONSIN–MADISON

Candidate for the degree of MS
Summer 2023

Rodenkirch, Benjamin Daniel

9068639617

Major: *Atmospheric and Oceanic Sciences MS*

The undersigned report that all degree requirements have been met on *Friday, May 12, 2023*. We recommend that the above named candidate be awarded the degree indicated.

Committee Member Name		Committee Member Signature	Date	
Rowe, Angela Kay	Advisor		14 June 2023	Reader
ADAMES-CORRALIZA, ANGEL			15 June 2023	Reader
L'ECUYER, TRISTAN S			6 June, 2023	Reader

☑ Student may continue for a PHD in the same program

☐ Student is required to deposit a thesis in Memorial Library

Abstract

Tropical oceanic convection (TOC) is a prevailing component of the tropical atmosphere and plays a significant role in modulating global weather and climate. Despite its importance, prediction challenges remain, partly attributed to a lack of understanding of TOC structure, initiation, and evolution, including how TOC relates to its near-storm environments. Prior studies suggest regionally dependent relationships between TOC structure and associated convective environments, necessitating targeted regional studies across the tropics. The NASA 2017 Convective Processes Experiment (CPEX) and 2021 CPEX Aerosols & Winds (CPEX-AW) field campaigns collected high-resolution measurements of three-dimensional (3-D) convective structure and convective environments in the Gulf of Mexico, Caribbean, and western Atlantic basins, providing the opportunity to investigate near-storm environmental relationships with 3-D TOC structure in a region lacking *in situ* non-tropical cyclone-related TOC research.

Utilizing collocated CPEX and CPEX-AW airborne datasets from the multi-wavelength Airborne Precipitation Radar (APR-3), Doppler Aerosol WiNd Lidar (DAWN), and dropsondes, large near-storm environmental variability existed both across TOC of similar convective type (i.e., isolated, organized) and within individual convective systems. However, trends still emerged amongst the large environmental variability. Two-dimensional (2-D) TOC structure was most consistently linked to planetary boundary layer (PBL) near-storm environments, with organized (i.e., multi-core) TOC being associated with generally greater PBL RH and vertical speed shear than isolated (i.e., single-core) TOC. TOC intensity (i.e., vertical TOC structure) was most commonly related to upper layer (i.e., above the freezing level) near-storm environments, with isolated TOC intensity

most consistently associated with upper layer CAPE and organized TOC intensity most consistently associated with upper layer RH. Synoptic-scale low-level convergence presence was also linked to greater TOC intensity in a detailed comparison of two convective systems with otherwise similar synoptic-scale setups and 2-D structures. Future work will extend regional analysis to the eastern Atlantic using NASA 2022 CPEX Cabo Verde (CPEX-CV) field campaign data. Idealized TOC simulations, satellite remote sensing observations, and NASA MERRA-2 reanalysis will also be analyzed to supplement and compare with the CPEX field campaign series *in situ* analysis.

Acknowledgements

I am incredibly fortunate to be surrounded by so many amazing people that have supported me during these past three years and throughout my life. First and most importantly, I would like to thank my advisor, Dr. Angela Rowe, for accepting me into her research group and providing invaluable guidance and support throughout my ongoing academic journey. She has provided me the opportunities of a lifetime, and her work ethic is truly inspirational. She is a great scientist, but most importantly, she is a great person. I also thank the other members of my advising committee, Dr. Tristan L'Ecuyer and Dr. Ángel Adames-Corraliza, for their valuable input and feedback for my research. Additionally, I am grateful for the exceptional faculty and staff at the AOS department, along with fellow students. Their intellect, drive, and kindness are inspiring and make the department as distinguished and welcoming as it is. I want to thank my family and friends for their love and support throughout the years and for encouraging my decision to return to school after a three-year hiatus working professionally. I am truly blessed to have all these people in my life, and without them I would not be where I am today.

This research was supported by NASA Award 80NSSC20K0894. I thank all NASA CPEX, CPEX-AW, and CPEX-CV participants, for which this research would not be possible without. I am especially grateful for all the wonderful people in mission management from the CPEX field campaign series for fostering such an inclusive and welcoming environment for everyone, especially students. I thank Randy J. Chase for providing APR-3 coding assistance, as well as Dr. Rosimar Rios-Berrios and Dr. George Bryan from NCAR for their ongoing help with the idealized tropical oceanic convection simulations.

Contents

List of Figures

List of Tables

Chapter 1

Introduction

Oceanic deep convection is a prevalent feature of the tropical atmosphere and plays a key role in driving both regional and global weather and climate. It highly influences the large-scale tropical atmospheric circulation through its redistribution of mass, momentum, heat, and moisture, while the precipitation, through buoyancy fluxes, instigates upper ocean responses (Alexander and Young, 1992; Brown and Zhang, 1997; LeMone et al., 1998; Saxen and Rutledge, 2000; Tompkins, 2001; Cetrone and Houze, 2006; Liu and Lian, 2010). Frequent, widespread three-dimensional (3-D) convective cloud structures significantly impact radiative fluxes, and thus enhanced warming/cooling, particularly near cloud-top levels (LeMone et al., 1998; Igel and van den Heever, 2015). Deep tropical oceanic convection (TOC) also frequently produces thermodynamically driven cold pools, which can trigger development of non-precipitating cumulus congestus clouds (a further radiative influencer), initiate new deep convection, alter planetary boundary layer (PBL) characteristics, and modify air-sea exchange (Chandra et al., 2018; Houze, 2018; Touzé-Peiffer et al., 2021).

With TOC modulating tropical weather and climate, accurate TOC representation and parameterization is critical for the success of weather and climate modeling efforts. However, despite decades of TOC research, challenges persist in modeling TOC. This challenge is partly attributed to a lack of understanding of TOC structure, initiation, and evolution, including how TOC relates to its near-storm environments throughout storm system lifecycle (Cetrone and

Houze, 2006; Igel and van den Heever, 2015; Minamide and Posselt, 2022). Studying near-storm environmental relationships is challenging, as it requires frequent, high-resolution measurements to capture fundamental small-scale convective processes, features, and environments. *In situ* data collection is the ideal means of garnering such measurements, and it is historically too few and far in between.

Observational analysis from field campaigns in the western Pacific basin (e.g., TOGA-COARE, KWAJEX, EMEX, PISTON) has sought to investigate near-storm environmental wind shear relationships with TOC structure using *in situ* dropsonde and radiosonde deployments. The west Pacific analyses have linked greater low-tropospheric speed shear to a greater degree of spatial organization of western Pacific mesoscale convective systems (MCSs) (Figure 1a), with quasi-linear convective systems oriented perpendicular to the low-level shear vector (Alexander and Young, 1992; LeMone et al., 1998; Chudler and Rutledge, 2021). Guy and Jorgensen (2014) found differing results in the Indian Ocean during the DYNAMO field campaign, with quasi-linear MCSs oriented more parallel to the low-tropospheric shear.

Strong deep-layer vertical speed shear in the western Pacific has been linked to larger, more intense linear precipitating systems (i.e., squall lines), owing to more expansive stratiform precipitation and anvil advection (Saxen and Rutledge, 2000). Research efforts using cloud-resolving model (CRM), spaceborne remote sensing, and European Centre for Medium-Range Weather Forecasts Reanalysis-Interim (ERA-Interim) reanalysis datasets have extended the regional, western Pacific observational analysis to the broad oceanic tropics and found similar deep-layer speed shear relationships with tropical squall lines (Tompkins, 2001) and tropical MCSs (Igel and van den

Heever, 2015) in general (Figure 2). However, Tompkins (2001) acknowledges CRM limitations (e.g., limited vertical dimension and unrealistic cyclic boundary conditions), while Igel and van den Heever (2015) acknowledges biases stemming from inherently inconsistent storm-relative CloudSat measurements.

While the aforementioned studies have made great strides towards understanding near-storm wind shear relationships with TOC structure, the research is predominately centered on (quasi-) linear convection. Non-linear TOC is abundant in the tropics (e.g., Houze et al., 2015) and warrants more targeted investigations. Additionally, the aforementioned studies are largely based in the western Pacific and Indian Ocean. With TOC structure varying across the tropics (Houze et al., 2015), an evaluation of TOC relationships with near-storm wind shear necessitates detailed *in situ* studies in other tropical oceanic regions.

Field campaign data in the western Pacific and Indian Ocean basins, along with broader tropical oceanic CRM and ERA-Interim reanalysis data, have also been used to investigate near-storm environmental moisture relationships with TOC structure. Analysis of these datasets have shown mid-tropospheric relative humidity (RH) to positively correlate with TOC precipitation area and intensity due to decreased dry air entrainment (Brown and Zhang, 1997; LeMone et al., 1998; Tompkins, 2001; Cetrone and Houze, 2006; Chen et al., 2017). Airborne data collected during DYNAMO over the Indian Ocean additionally showed lesser near-storm, mid-tropospheric moisture associated with isolated TOC to correspond to deeper convectively generated cold pools and, consequently, longer PBL recovery times (Savarin et al., 2014; Chen et al., 2016). However, the relationships between lower-tropospheric moisture and TOC precipitation area and intensity

vary, in both strength and sign, across tropical oceanic studies, even within similar regions (Tompkins, 2001; Cetrone and Houze, 2006; Chen et al., 2017). The inconsistencies may relate to data collection during differing TOC lifecycle stages, with low-level inflow shown to potentially be more important during early lifecycle stages compared to mid-level inflow for later lifecycle stages (Mechem et al., 2002).

Similarly, inconsistent relationships between environmental CAPE and TOC structure exist across prior studies of the western Pacific basin. Cetrone and Houze (2006) and Chudler and Rutledge (2021) found KWAJEX and PISTON MCSs, respectively, to be associated with lesser CAPE compared to smaller, less organized convective systems (Figure 1b), while Kingsmill and Houze (1999) found opposing results using TOGA-COARE data. The conflicting results could stem from thermodynamic instability being asymmetrically concentrated in the lower troposphere in the KWAJEX soundings and near-surface modification by MCSs in the PISTON soundings, thereby negatively biasing CAPE measurements near the MCSs (Cetrone and Houze, 2006; Chudler and Rutledge, 2021).

Collectively, both the strength and sign of near-storm mean-layer environmental moisture, wind shear, and CAPE relationships with TOC structure are inconsistent across studies. These inconsistent findings could be attributed to a multitude of factors, like differing analysis methods and data sources. However, a lack of regional context may be a major culprit. Most modern studies of environmental relationships with non-tropical cyclone related TOC structure are focused in the western Pacific or broadly across the oceanic tropics. This lack of modern, regionally diverse, and regionally distinct research is an issue because TOC structure and its relationships with near-storm

environments have been shown through TRMM observations and ERA-Interim reanalysis to exhibit regional dependencies (Figure 3) (Houze et al., 2015; Chen et al., 2017). Synoptic-scale climatological differences, such as sea surface temperature distribution, jet presence, and MJO influences, likely play a role in these regional dependencies by influencing TOC initiation, organization, and microphysics. Therefore, evaluations of TOC structure relationships with near-storm environments necessitate targeted regional studies, particularly in understudied areas, so that the impacts of region-relative enhanced/diminished mean-layer moisture and wind shear can be assessed (Cetrone and Houze, 2006). Satellite and reanalysis datasets provide the ability to examine each tropical oceanic region separately, but their limited spatial and temporal resolutions cannot sufficiently capture essential small-scale near-storm environmental variability and convective processes. Consequently, targeted regional *in situ* studies equipped with collocated high-resolution hydrometeor, moisture, and wind measurement capabilities are imperative to adequately analyze near-storm environmental relationships with TOC structure.

Two such targeted *in situ* regional studies were the 2017 NASA Convective Processes Experiment and 2021 CPEX – Aerosols & Winds (CPEX-AW) field campaigns based in Ft. Lauderdale, Florida and St. Croix, USVI, respectively. CPEX and CPEX-AW performed a total of 23 science flights (Figure 4) aboard the NASA DC-8 research aircraft from 27 May 2017 – 24 June 2017 and 20 August 2021 – 4 September 2021, respectively, to study TOC processes in the Gulf of Mexico, Caribbean Sea, and western Atlantic—regions that were notably lacking recent *in situ*, non-tropical cyclone related deep convective research (Cui et al., 2020). The DC-8 aircraft was equipped with, amongst other instrumentation, a multi-wavelength airborne precipitation radar, a Doppler wind lidar, and dropsondes (Figure 5). Together, these instruments provided rare, coincident, high-

resolution profiling of 3-D convective structure, near-cloud winds, and near-storm moisture for convective systems of different spatial scales and intensities (Turk et al., 2020; Hristova-Veleva et al., 2021). Given the uniqueness of this suite of observations, the CPEX and CPEX-AW field campaigns present an exceptional opportunity to analyze their region's near-storm environmental relationships with tropical oceanic 3-D convective structure, which will be the focus of this study. In particular, ***how does 3-D TOC structure relate to near-storm environmental RH, vertical speed shear, and CAPE in different tropospheric vertical layers in the CPEX(-AW) observational domain?***

Prior studies suggest the strength and sign of these environmental relationships may be layer-dependent. The three aforementioned DC-8 instruments' high vertical resolutions provide sufficiently numerous observations in any given tropospheric layer to adequately assess multiple tropospheric layers' environmental characteristics. We hypothesize that larger, more intense (i.e., more organized) TOC will be associated with greater near-storm mean RH in each defined tropospheric layer, due to less dry air entrainment into the convective system (i.e., less evaporative cooling, limiting cold pool development, and less negative buoyancy introduction) (Brown and Zhang, 1997; Savarin et al., 2014; Chen et al., 2016). Similar to western Pacific field campaign analysis, more organized, multi-core convection in the CPEX(-AW) domain is also hypothesized to be connected to greater near-storm mean vertical speed shear in each defined tropospheric layer, due to more effective separation of convective updrafts and downdrafts and continued initiation along cold pool boundaries (Yuter and Houze, 1995; Houze, 2018). Conflicting arguments in the literature make it difficult to predict how CAPE will relate to 3-D TOC structure. Some studies link lesser CAPE to more organized convection (Cetrone and Houze, 2006; Chudler and Rutledge,

2021), while other studies link greater CAPE to more organized convection (e.g., Kingsmill and Houze, 1999). Meanwhile, an argument exists that CAPE does not correlate with TOC structure at all, due to typically small CAPE variations within a given tropical oceanic region for a given time of year (Lucas et al., 1994). Therefore, it is unclear what we expect with regards to CAPE relationships with 3-D TOC structure in the CPEX(-AW) domain, and it will be interesting to evaluate the results.

To address the research question and evaluate the associated hypotheses, the organization of the paper is as follows. Section 2 offers a description of the CPEX(-AW) instrumentation and data used for the analysis. Section 3 outlines the methods used to filter and contextualize the observational data, along with the approaches and techniques used to analyze 3-D TOC structure and its near-storm environments. Section 4 introduces and discusses the results of the analysis of near-storm, mean-layer environmental relationships with 3-D TOC structure in the CPEX(-AW) region, first by comparing convective systems with notably different 3-D structure (e.g., single-core vs. multi-core) and then by comparing convective systems with similar 3-D structure (e.g., multi-core vs. multi-core). Section 5 provides a discussion of the results in the context of prior field campaign studies from different tropical oceanic regions. Section 6 concludes the paper with main takeaways from the analysis and next steps for future research.

a) Figures

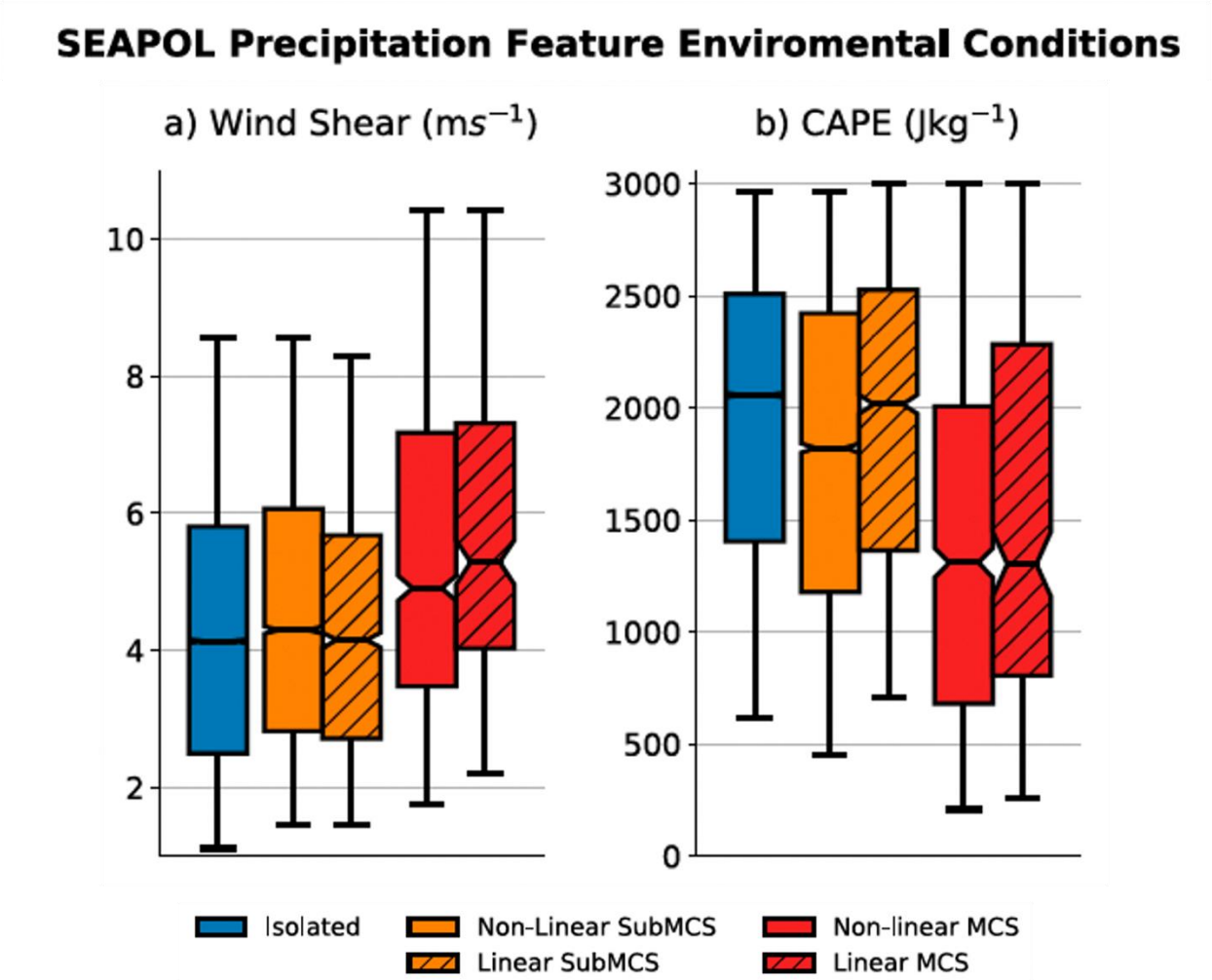

Figure 3: (a) 1000 – 850 mb speed shear and (b) CAPE for different TOC structures observed during the Propagation of Intraseasonal Oscillations (PISTON) field campaign in the western tropical North Pacific in 2018 and 2019. Values derived from atmospheric soundings. Adapted from Chudler and Rutledge (2021).

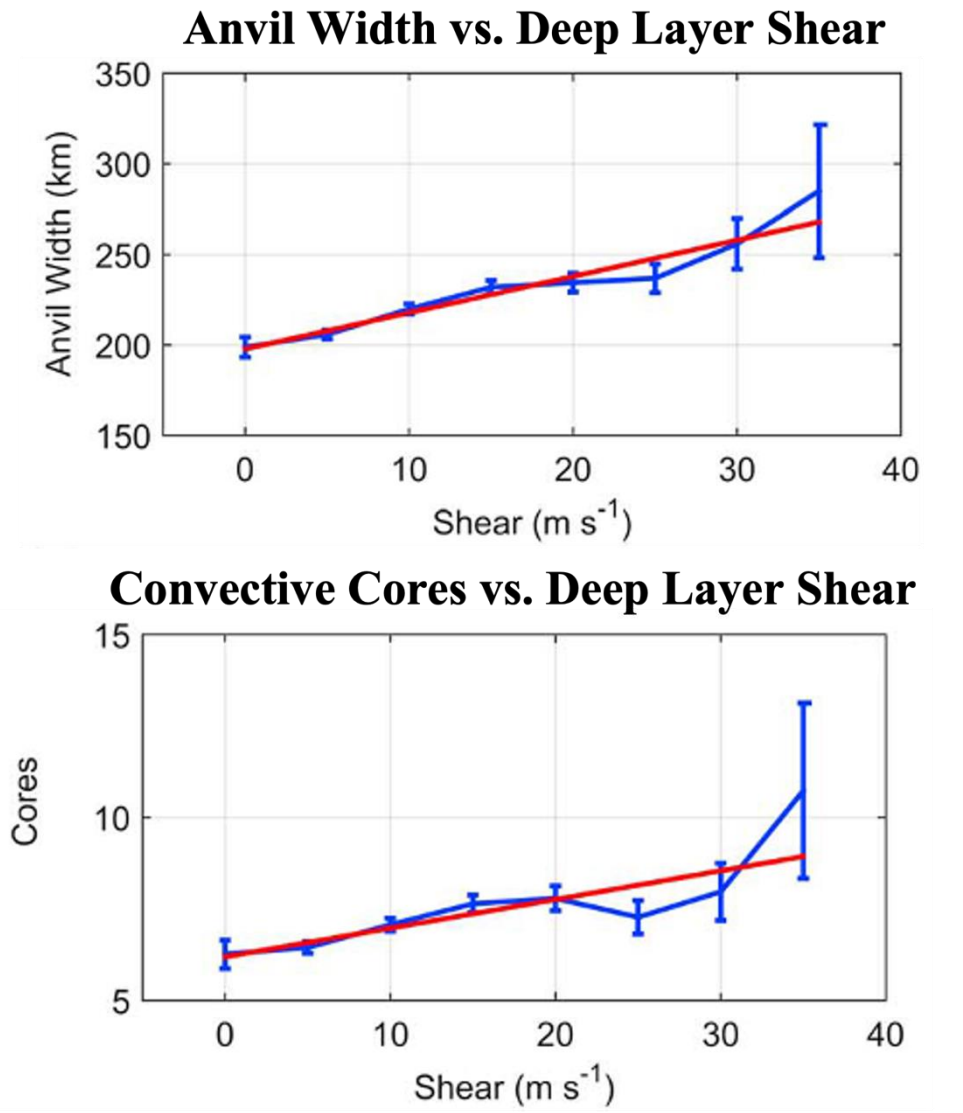

Figure 4: Mean (top) anvil width and (bottom) number of cores of deep tropical convection as a function of vertical speed shear (5 m s^{-1} width bins). The error bars represent the 95% confidence interval for the mean of each bin. Linear regressions for the unbinned data are in red. Adapted from Igel and van den Heever (2015).

Region	TPWV (mm)	RHLow (%)	RHMid (%)	Shallow wind shear ($m\,s^{-1}$)	Deep wind shear ($m\,s^{-1}$)	CIN ($J\,kg^{-1}$)	CAPE ($J\,kg^{-1}$) ($\times 10^3$)	LCL (km)
Tropical ocean	57.8	89.0	75.7	4.0	9.7	7.9	1.12	0.40
	47.1	84.1	47.6	3.6	10.8	8.6	1.06	0.54
INOC	57.4	88.6	78.9	3.5	9.0	7.0	1.1	0.42
	51.4	84.7	60.3	3.3	8.7	7.9	1.2	0.53
GATE	55.7	90.7	72.2	4.4	8.7	6.3	0.8	0.37
	51.1	87.4	57.6	4.1	8.8	7.6	0.9	0.47
EPAC	56.8	92.0	70.3	4.6	9.8	6.3	0.8	0.32
	50.4	88.4	53.2	4.0	10.4	7.4	0.9	0.43
WPAC	59.6	87.9	78.5	3.3	7.8	9.3	1.3	0.44
	53.6	83.9	58.7	3.1	7.1	11.0	1.4	0.55
BBL	63.2	87.2	83.6	3.9	13.4	8.8	1.6	0.41
	58.5	84.4	70.4	3.3	11.4	9.8	1.6	0.5

Figure 5: Mean environmental metrics for TOC with rain area greater than 10^4 km^2 (top row) and rain area less than 100 km^2 (bottom row) for each tropical oceanic region. INOC = Indian Ocean, GATE = Eastern Atlantic, EPAC = East Pacific, WPAC = West Pacific, BBL = Bay of Bengal. TOC observed by TRMM radar and environmental metrics derived from 1.5° grid ERA-Interim reanalysis. From Chen et al. (2017).

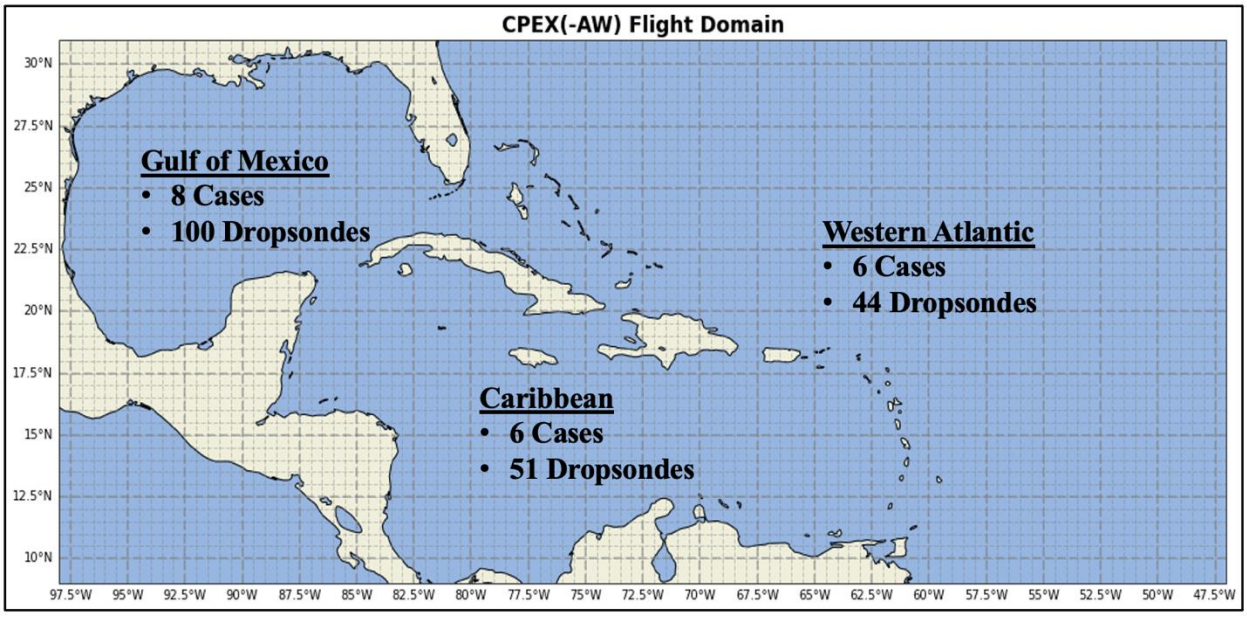

Figure 6: Number of TOC systems (cases) sampled by the CPEX (2017) and CPEX-AW (2021) field campaigns combined in each given region, along with the number of associated dropsondes.

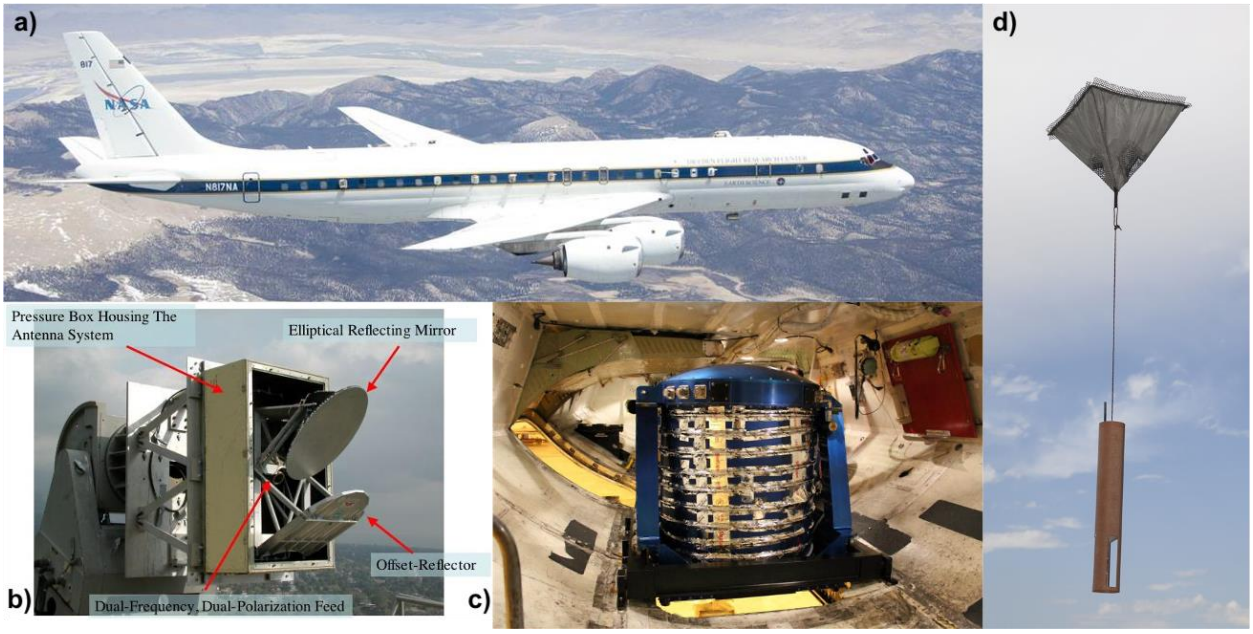

Figure 5: (a) NASA DC-8 aircraft, (b) Third-Generation Airborne Precipitation Radar (APR-3), (c) Doppler Aerosol WiNd Lidar (DAWN), and (d) dropsonde instrumentation used during the CPEX and CPEX-AW field campaigns to sample TOC and their near-storm environments (Images source: NASA).

Chapter 2

Data

a) CPEX and CPEX-AW Overview

The NASA DC-8 aircraft was equipped with six science instruments during CPEX and five during CPEX-AW. These instruments included three microwave sounders (the High Altitude MMIC Sounding Radiometer (HAMSR), Microwave Atmospheric Sounder for Cubesat (MASC, CPEX only), and Microwave Temperature & Humidity Profiler (MTHP, CPEX only) and the aerosol and water vapor profiling High Altitude Lidar Observatory (HALO, CPEX-AW only). This paper will focus on analysis of the higher spatial resolution airborne datasets from the following instrumentation: dropsondes, the Doppler Aerosol WiNd Lidar (DAWN), and the Third-Generation Airborne Precipitation Radar (APR-3). Together, these three instruments provided coincident, detailed measurements of near-storm moisture, winds, and 3-D convective structure (e.g., Figure 6) at sufficient resolutions to analyze characteristics of distinct vertical layers. Seventeen of the 23 CPEX(-AW) science flights sampled 20 separate convective systems (hereafter referred to as convective cases; Figure 4) with this instrument payload. As such, only observational data from these 17 science flights were used for analysis for this paper.

b) Dropsondes

Vertical profiles of pressure, temperature, horizontal wind velocity, and humidity were collected throughout the CPEX science flights using Yankee Environmental Systems' (YES) eXpendable

Digital Dropsondes (XDDs) (Figure 5; CPEX Dropsonde, 2019; Black et al., 2017). The YES XDDs use the High-Definition Sounding System (HDSS) dropsonde system developed by the Office of Naval Research (ONR) (CPEX Dropsonde, 2019; Black et al., 2017). The CPEX dropsondes sampled pressure at a rate of 2-Hz, accuracy of 1.5 mb (at 25°C), and resolution of 2.5 mb (Greco et al., 2018; Black et al., 2017). Temperature was collected at a 2-Hz rate with an accuracy of 0.148°C and resolution of 0.0168°C (Greco et al., 2018; Black et al., 2017). Horizontal wind velocity was sampled at a rate of 4-Hz, accuracy of 0.5 m s^{-1}, and precision of 0.2 m s^{-1} (Greco et al., 2018; Black et al., 2017). RH was collected at a 2-Hz rate, with an accuracy of 1.8% (at 25°C) and resolution of 0.1% (Greco et al., 2018; Black et al., 2017). For CPEX-AW, vertical profiles of pressure, temperature, horizontal wind velocity, and humidity were collected using National Center for Atmospheric Research (NCAR) dropsondes. The NCAR dropsondes use the Airborne Vertical Atmospheric Profiling System (AVAPS) developed by Vaisala Inc. (AVAPS Dropsondes, 2023). The CPEX-AW dropsondes sampled pressure with an accuracy of 0.5 mb and resolution of 0.01 mb (AVAPS Dropsondes, 2023). Temperature was collected with an accuracy of 0.2°C and resolution of 0.01°C (AVAPS Dropsondes, 2023). Horizontal wind velocity was sampled with an accuracy of 0.5 m s^{-1} and resolution of 0.01 m s^{-1} (AVAPS Dropsondes, 2023). RH was collected with an accuracy of 3% and resolution of 0.01% (AVAPS Dropsondes, 2023).

Given the scales that are being explored for comparing mean-layer wind shear and RH (differences hypothesized to be several m s^{-1} and several percent, respectively), the CPEX(-AW) dropsonde accuracies and precisions for each metric are sufficient for the purposes of this study. RH accuracies were notably worse in actively precipitating environments as the dropsondes exhibited moisture biases when encountering precipitation, likely due to water ingress (Greco et al., 2018).

As such, moisture data from dropsondes deployed in actively precipitating environments was excluded from analysis in this paper. The dropsonde data was processed using the NCAR Atmospheric Sounding Processing ENvironment (ASPEN) software, which, amongst other quality control practices, removes outlier data and smooths profiles accordingly (Greco et al., 2018; Vömel et al., 2021; Martin and Suhr, 2021). Post-mission GPS correction was also employed (CPEX Dropsonde, 2019).

Data for which the dropsonde fall speed did not exceed 15 m s^{-1} was filtered out, and usage of hydrostatic altitude, when available, was prioritized over GPS altitude due to greater height accuracy (CPEX Dropsonde, 2019). Temperature, relative humidity, dewpoint, and both component wind values all had to be present for the dropsonde data to be included at a given height level. Dropsonde profiles with frequent, graphically visible anomalous spikes in equivalent potential temperature were excluded from further analysis. In total, this filtering amounted to 195 usable dropsondes across the 20 convective cases (Figure 4).

c) Doppler Aerosol WiNd Lidar (DAWN)

High-resolution vertical profiles of wind near convection were collected by the DAWN instrument aboard the NASA DC-8 aircraft during CPEX(-AW) (Figure 5; Kavaya et al., 2014; Greco et al., 2020). DAWN is equipped with a 2-μm, 10-Hz laser that utilizes atmospheric aerosols to measure horizontal wind components (Kavaya et al., 2014; Turk et al., 2020; Greco et al., 2020). The laser scanned conically 30° off nadir, collecting two 66 m resolution line-of-sight (LOS) wind profiles at -45° and 45° azimuth angles relative to the flight direction (CPEX DAWN, 2019; Turk et al., 2020). DAWN vertical wind profiles were obtained at horizontal resolutions as fine as 3-7 km and

a vertical resolution of ~33 m using the LOS wind profiles (CPEX DAWN, 2019; Greco et al., 2020). DAWN profiles were severely attenuated when encountering opaque clouds (e.g., convective anvil cirrus), and data gaps frequently existed in the mid-troposphere due to low aerosol concentrations, as DAWN relies upon sufficient aerosol presence to measure wind velocity (Bedka et al., 2021). DAWN wind speed accuracy was < 0.05 m s^{-1}, while wind speed precision was < ~1.5 m s^{-1} (Greco et al., 2020). DAWN winds also showed a low bias of < 0.20 m s^{-1} with the dropsonde winds (Greco et al., 2020). Given the scales that are being explored for comparing mean-layer wind shear (differences hypothesized to be several m s^{-1}), the DAWN wind accuracy and precision are adequate for the purposes of this study.

DAWN data was processed via methods described in Kavaya et al. (2014) and Greco et al. (2020). In layers of low signal-to-noise ratio (SNR), the Adaptive Signal Integration Algorithm (ASIA) was employed to enhance vertical profile coverage (CPEX DAWN, 2019; Greco et al., 2020; Bedka et al., 2021). Wind data collected during aircraft banking that exceeded 1.5° was excluded, as was wind data sampled during aircraft ascents/descents greater than 7 m s^{-1} (CPEX DAWN, 2019). Both component wind values had to be present for the DAWN data to be included at a given height level (defined as above mean sea level). The lowest available integration index—with the lowest possible integration index being the baseline profile data and higher integration indices increasingly incorporating ASIA—for each height level was used, as suggested by CPEX DAWN (2019).

d) Third-Generation Airborne Precipitation Radar (APR-3)

Vertical radar reflectivity profiles of 3-D convective hydrometeor structure were collected using the APR-3 instrument (Figure 5; Sadowy et al., 2003). APR-3 mirrors the Global Precipitation Measurement Mission Dual-Frequency Precipitation Radar (GPM-DPR) 13.4-GHz (Ku-) and 35.6 GHz (Ka-) bands, which simultaneously measure co- and cross-polarized reflectivities and vertical Doppler velocities (Durden et al., 2012; Turk et al., 2020; CPEX APR-3, 2018). APR-3 scans cross-track with a 50° swath (+/- 25° from nadir), a 10-km ground swath, and a vertical resolution of 60 m for both frequency bands (Sadowy et al., 2003; Durden et al., 2012). Ku-band horizontal resolution is ~730 – 800 m at 10-km altitude with a 10 dBZ sensitivity, while Ka-band horizontal resolution is ~920 – 1000 m at 10-km altitude with a -10 dBZ sensitivity (Sadowy et al., 2003; Durden et al., 2012). The Ku-band can measure a maximum unambiguous Doppler velocity of +/- 27.5 m s^{-1}, while the Ka-band can measure a maximum unambiguous velocity of +/- 10.5 m s^{-1} (CPEX APR-3, 2018). Doppler velocity precisions for the Ku- and Ka-bands are 0.3 – 0.4 m s^{-1} and 1.0 m s^{-1}, respectively (Sadowy et al., 2003; Durden et al., 2012).

APR-3 data was processed via methods described in Durden et al. (2012), which includes Ku-band calibration using clear air ocean surface observations and Ka-band calibration via comparison with Ku-band reflectivities in a stratiform precipitation scene. Ku- and Ka-band reflectivity calibration uncertainties for the CPEX campaign were estimated at 1 dB and 1.5 dB, respectively (CPEX APR-3, 2018; Turk et al., 2020; Durden et al., 2012).

Only profiles from the pseudo-nadir ray of each APR-3 cross-track scan were utilized in subsequent analysis because these profiles captured the vertical convective structure directly below

the aircraft and thus better aligned with DAWN and dropsonde profiles. The pseudo-nadir ray is defined as the APR-3 scan's ray for which the difference between the ray incidence angle and the aircraft roll angle is minimized. This method thereby selects the ray that vertically scans closest to directly below the aircraft. Furthermore, only Ku-band reflectivity profiles were used for analysis, as the Ku-band captures precipitation structure better than the Ka-band, which is more quickly attenuated by precipitating hydrometeors. Doppler velocity datasets were corrupted for a majority of CPEX convective cases (i.e., cases prior to 16 June 2017). Therefore, Doppler velocity was not incorporated in subsequent analysis.

e) Figures

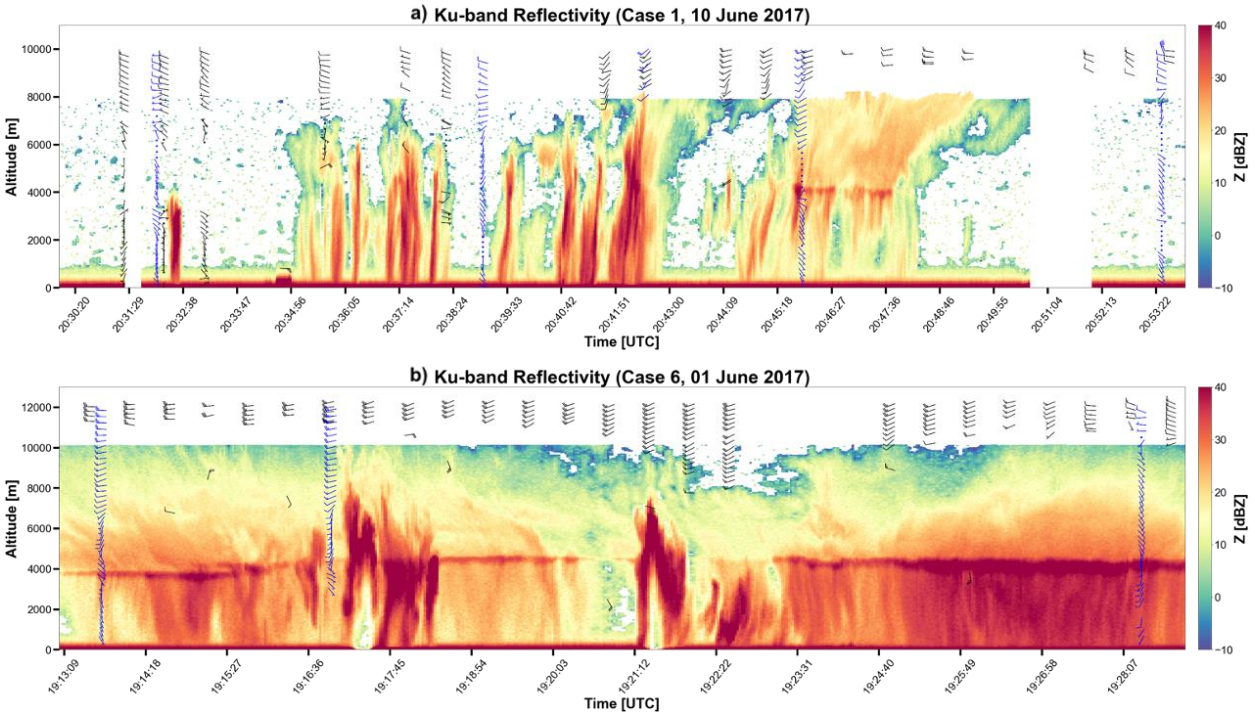

Figure 6: APR-3 Ku-band reflectivity profiles (fill), dropsonde wind profiles (blue barbs), and DAWN wind profiles (black barbs) for an (a) isolated and (b) organized TOC system observed during CPEX.

Chapter 3

Methods

a) Convective Case Characterization

In order to investigate near-storm environmental relationships with TOC structure, each of the 20 CPEX(-AW) convective cases was categorized as either isolated, organized, or scattered based on horizontal precipitation extent and continuity provided by archived hourly Integrated Multi-satellitE Retrievals for GPM (IMERG) satellite data. Given the inherent small number of cases from the field campaigns, categorization of each convective system was manual. Isolated convective systems were defined as horizontally small, cellular precipitating regions, while organized convective systems were defined as broader, continuous, multi-core precipitating regions. Scattered convection was defined as broad, discontinuous precipitating regions. An example of each type of convection in the context of IMERG is depicted in Figure 7. The focus of this paper is on isolated and organized non-tropical cyclone TOC cases. As such, 12 out of the 20 total convective cases sampled during CPEX(-AW) underwent further analysis (Table 1). Two scattered convective cases were omitted due to non-distinct cellular nor multi-core horizontal precipitation structures. Additionally, six organized convective cases were omitted due to association with tropical cyclones (including tropical depressions). All but one (i.e., Case 15) of the qualifying 12 cases was sampled during a similar time of day (i.e., between 1800 UTC and 0000 UTC), so diurnal influences on convective structure are assumed to have been similar for each case.

b) Dropsonde Characterization

Only dropsonde profiles temporally collocated with their respective qualifying convective case's APR-3 data (i.e., within or near the anvil region) were considered for analysis, amounting to 111 dropsondes. Each dropsonde from the cases identified in Table 1 was characterized by the convective type of its respective case, along with the convective-relative environment it was deployed into. Using APR-3 plots overlaid with dropsonde and DAWN wind profiles (e.g., Figure 6), the three environmental categories were "Clear" (little to no reflectivity overlaid with the profile), "In Cloud" (deployed through a non-precipitating cloud layer(s)), and "In Precip" (deployed through an actively precipitating region). For example, the dropsonde around 2032 UTC in Figure 6a was characterized as "Clear", while the dropsonde near 2045 UTC was categorized as "In Precip". Similarly, all three dropsondes in Figure 6b were labeled as "In Precip". Skew-T diagrams of the dropsonde profiles also aided in validation of the environmental categorization. For example, the environment of the dropsonde near 2039 UTC in Figure 6a appears to be "Clear". However, the dropsonde's skew-T diagram in Figure 8 denotes a deep saturated layer from 1000 mb – 650 mb, indicative of an "In Precip" environment. The distribution of dropsondes amongst the three environmental categories for each case is shown in Table 1, along with the distribution of full and partial (i.e., sparse data coverage in certain layers) dropsonde profiles for each case. Due to the notable moisture biases of "In Precip" dropsondes, as previously mentioned in Section 2, only wind data from "In Precip" dropsondes was used for analysis in this paper.

Each dropsonde was also characterized by convective lifecycle stage at the time of deployment (see Table 1), as near-storm environments can vary with the maturity of convective systems. The convective lifecycle stage for each dropsonde was deemed to be "growing", "mature", or

"weakening" based on APR-3 reflectivity features near the dropsonde profile (e.g., stratiform brightband strength, presence of embedded convective elements) and convective core evolution using archived hourly GOES-East IR COLOR imagery. Together, the three separate dropsonde categorizations provided storm-relative temporal and environmental context for analysis of near-storm environmental relationships with convective type. It is noted that all near-storm environmental analysis was performed for data from all convective lifecycles and separately excluding dropsondes from the weakening lifecycle stage. Excluding the weakening lifecycle stage was tested as a means to focus on environments supporting convective development and sustainment. However, the results of the analysis excluding the weakening lifecycle stage data (figures not shown in this paper) were similar to the results of the analysis that included data from all lifecycle stages.

c) Mean-layer, Near-storm Environmental Metrics

Mean relative humidity (RH) and vertical wind speed shear were calculated for each dropsonde profile for four distinct layers: the PBL, mid layer, upper layer, and deep layer (Figure 9). The base of the PBL is defined as the profile height nearest to the surface, ranging from 6.5 m to 338.5 m because of dropsonde transmission issues. Metric values were not found to correlate with near-surface height within that range. The top of the PBL is defined as the first height for which the virtual potential temperature exceeds its value nearest to the surface by 0.5 °C (e.g., Blumberg et al., 2017). The mid layer extends from the top of the PBL up to the freezing level (i.e., 0 °C), while the upper layer extends from the freezing level up to the lowest maximum height of the 111 qualifying dropsondes (7622.5 m), such that a uniform upper layer cap was achieved. The deep

layer ranges from the profile height nearest to the surface up to the lowest maximum dropsonde height.

Layer RH calculations use RH data at all height levels within the specified layer thresholds to calculate profile mean-layer RHs. With the assistance of the Sounding/Hodograph Analysis and Research Program in Python (SHARPpy; Blumberg et al., 2017) open-source meteorological package, vertical speed shear was calculated for the four distinct layers using the dropsonde component winds at each layer threshold height (interpolated as necessary). In addition to mean-layer RH and vertical speed shear, both most-unstable convective available potential energy (MUCAPE, using the most unstable air parcel found within the lowest 300-mb of the troposphere) and mixed-layer CAPE (MLCAPE, using a parcel with the mean temperature and moisture values from the lowest 100-mb of the troposphere) were calculated for each dropsonde for the deep layer and the upper layer (i.e., above the freezing level) using SHARPpy. Upper layer CAPE supplements deep layer CAPE as an effort to avoid potential negative biasing of near-storm CAPE measurements by MCSs, as previously discussed with Chudler and Rutledge (2021). Environmental metrics for layers that were not fully sampled by partial dropsonde profiles (see Table 1) were excluded from analysis.

Similar to the dropsonde data, only DAWN profiles that were temporally collocated with their respective convective case's APR-3 data—and thus near convection—were included in analysis. The DAWN instrument provided much denser wind profiling (both spatially and temporally) in non-anvil regions compared to the dropsondes. That being said, PBL depth and freezing level height could not be identified for each DAWN profile owing to temperature and moisture data not

available from DAWN. With PBL depth in dropsonde data found to vary appreciably within short geospatial and temporal ranges, only deep layer wind shear could be confidently calculated for the DAWN profiles. The DAWN deep layer, in comparison with the dropsonde deep layer, was similarly capped at the lowest maximum dropsonde height of 7622.5 m. However, the deep layer for the DAWN data slightly varies from the dropsonde deep layer, in that a uniform near-surface value of 500 m was employed to omit low SNR (i.e., noisy) data from DAWN shear calculations. For similar reasons, DAWN profiles, with a vertical resolution of ~33 m, were also required to contain at least 20 data points within the lowest 1 km of the atmosphere.

DAWN deep layer vertical wind shear was calculated using the component wind data closest to each deep layer threshold height, with the component winds required to be within 80 m of the deep layer threshold heights. To assure that single-point wind shear calculations were not being affected by potentially isolated anomalous and/or spurious wind data, DAWN wind shear was also calculated using both the median and mean component wind values out of the three nearest data points to each deep layer threshold height. Each of the three data points was required to be within a 160 m height delta of the deep layer threshold heights, with the 160 m height delta informed by the CPEX minimum PBL depth of 161.8 m. The single-point, median, and mean wind shear calculation methods produced near identical shear values, providing confidence in using the single-point method. After DAWN deep layer wind shear was calculated, an equivalent 500 m – 7622.5 m dropsonde deep layer shear was computed for direct comparison with DAWN deep layer shear.

d) Dropsonde Median Ku-band Reflectivity Profiles

To analyze potential links between near-storm, mean-layer environmental parameters and convective intensity, median APR-3 Ku-band reflectivity profiles were constructed for each dropsonde and matched with their associated dropsonde mean-layer metrics. These median reflectivity profiles were calculated from the collection of all Ku-band profiles within a 10-min temporal proximity (20-min total time delta) to a given dropsonde. The 5-, 7.5-, and 12.5-min time deltas were also considered for the median reflectivity profile calculation, but the 10-min time delta was ultimately chosen, as it captured brightband signatures while minimizing noise (Figure 10). APR-3 data below 1.5 km was excluded to avoid inclusion of potentially spurious near-surface data (Sadowy et al., 2003; Durden et al., 2003). The In Precip dropsondes were omitted from the median reflectivity profile analysis with near-storm mean-layer RH and CAPE due to known dropsonde moisture biases in actively precipitating regions during the CPEX(-AW) campaigns (Greco et al., 2018).

e) Contoured Frequency by Altitude Diagrams

For analysis of convective intensity and the reflectivity features of each convective case, all APR-3 Ku-band reflectivity profiles for a given case were binned into 2-dimensional histograms with 5-dBZ and 0.5-km intervals to create Contoured Frequency by Altitude Diagrams (CFADs) (Yuter and Houze, 1995). The reflectivity bins extend from -20 dBZ to 60 dBZ. The height bins extend from 1.5 km to 8 km, so as to omit potentially attenuated near-surface data (Sadowy et al., 2003; Durden et al., 2003) and provide a uniform upper layer altitude cap to allow for case intercomparison. The heights from the reflectivity profiles, and thus in each CFAD, were not adjusted for brightband height, as brightband height across all the convective cases did not vary

considerably. Each CFAD was normalized by the maximum bin count in any height interval, allowing for frequency comparisons across height levels (e.g., Zagrodnik et al., 2019). Each CFAD was separately normalized by the maximum bin count in each height interval, allowing for easier frequency comparisons at a given height level. Subsequent so-called “difference CFADs” were produced by subtracting one case’s normalized CFAD from another. These difference CFADs allow for investigation of convective intensity and storm structure differences between cases with distinct mean-layer environmental metric differences (Yuter and Houze, 1995). Convective case intercomparisons, via difference CFADs, were only performed between cases of similar convective type (i.e., isolated vs. isolated, organized vs. organized), as comparisons across convective type would offer little value due to inherent differences in cellular vs. multi-core storm structure. Convective case intercomparisons were also only performed between cases that were observed during a similar convective lifecycle stage, such that predominantly convective elements are not compared with predominantly stratiform elements.

f) Figures and Tables

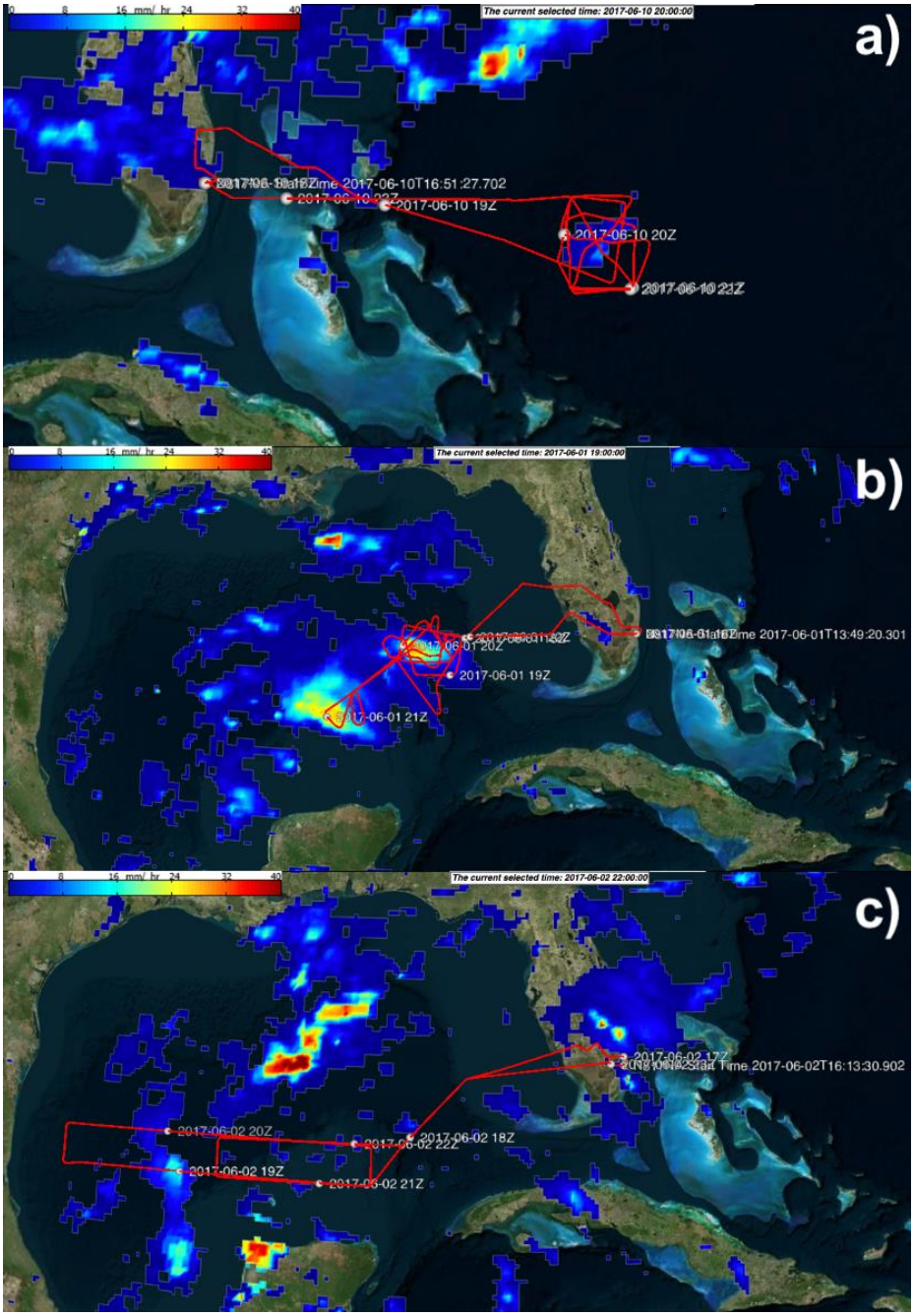

Figure 7: An example of (a) isolated, (b) organized, and (c) scattered TOC sampled during CPEX, as defined by GPM IMERG precipitation area and continuity. CPEX science flight tracks are overlaid in red with hourly timestamps.

Table 2: CPEX and CPEX-AW convective cases used for analysis in this study. The number of associated dropsondes (full and partial) is included for each case, along with dropsonde distribution by the environment it was deployed into and the lifecycle stage of the convection at the time of the dropsonde's deployment.

Case	Date	Field Campaign	Region	Convective Type	Number of Dropsondes (Full)	Number of Dropsondes (Partial)	Clear	In Cloud	In Precip	Growing	Mature	Weakening
1	20170610	CPEX	Western Atlantic	Isolated	11	2	9	3	1	0	10	3
2	20170624	CPEX	Caribbean	Isolated	1	2	3	0	0	2	1	0
3	20170624	CPEX	Gulf of Mexico	Isolated	4	0	3	1	0	2	2	0
15	20210822	CPEX-AW	Western Atlantic	Isolated	2	1	2	1	0	0	0	3
4	20170615	CPEX	Caribbean	Organized	2	2	0	3	1	0	4	0
5	20170616	CPEX	Caribbean	Organized	3	16	0	0	19	0	9	10
6	20170601	CPEX	Gulf of Mexico	Organized	6	12	0	1	17	0	11	7
7	20170606	CPEX	Gulf of Mexico	Organized	4	2	4	0	2	0	6	0
8	20170617	CPEX	Caribbean	Organized	0	8	2	0	6	0	8	0
13	20170611	CPEX	Gulf of Mexico	Organized	15	4	10	5	4	5	12	2
14	20210821	CPEX-AW	Western Atlantic	Organized	1	4	4	1	0	0	5	0
16	20210824	CPEX-AW	Caribbean	Organized	4	5	4	0	5	0	5	4

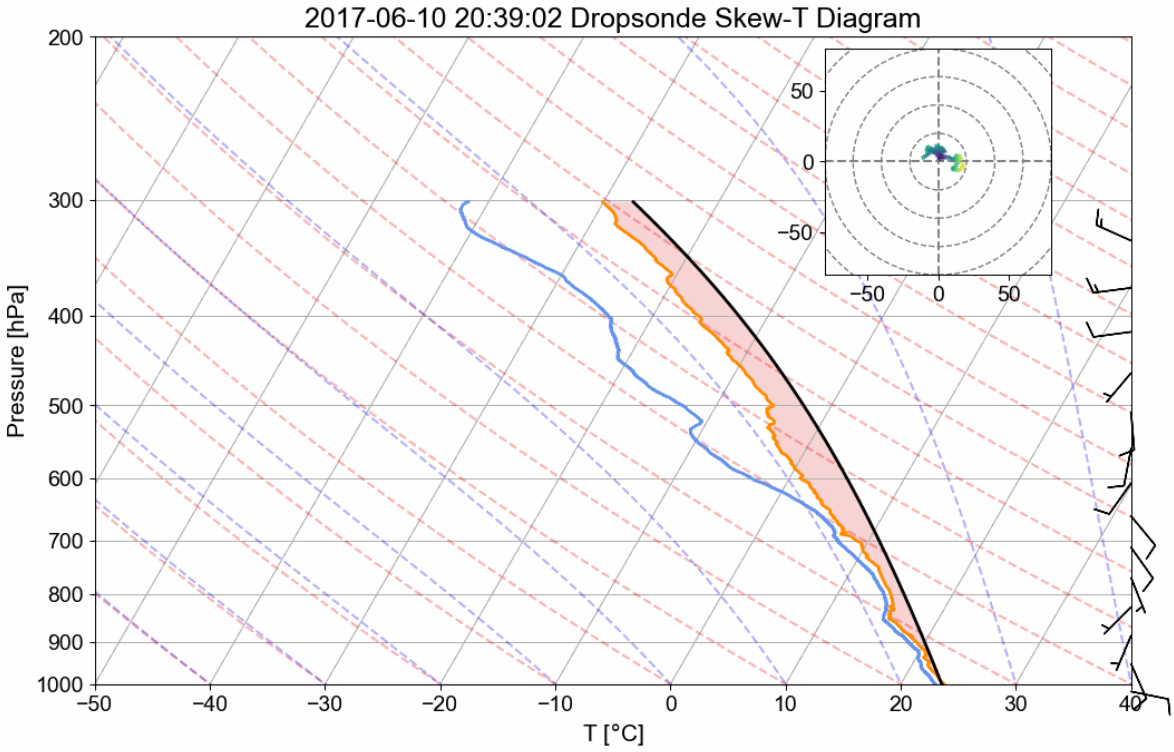

Figure 8: Skew-T diagram and hodograph for a dropsonde from Case 1 (20:39:02 UTC). The saturated 1000 mb – 650 mb layer is indicative of an actively precipitating environment. CAPE is shaded in light red, and wind barbs are provided on the right hand side (full lines = 5 m s^{-1}, half lines = 2.5 m s^{-1}).

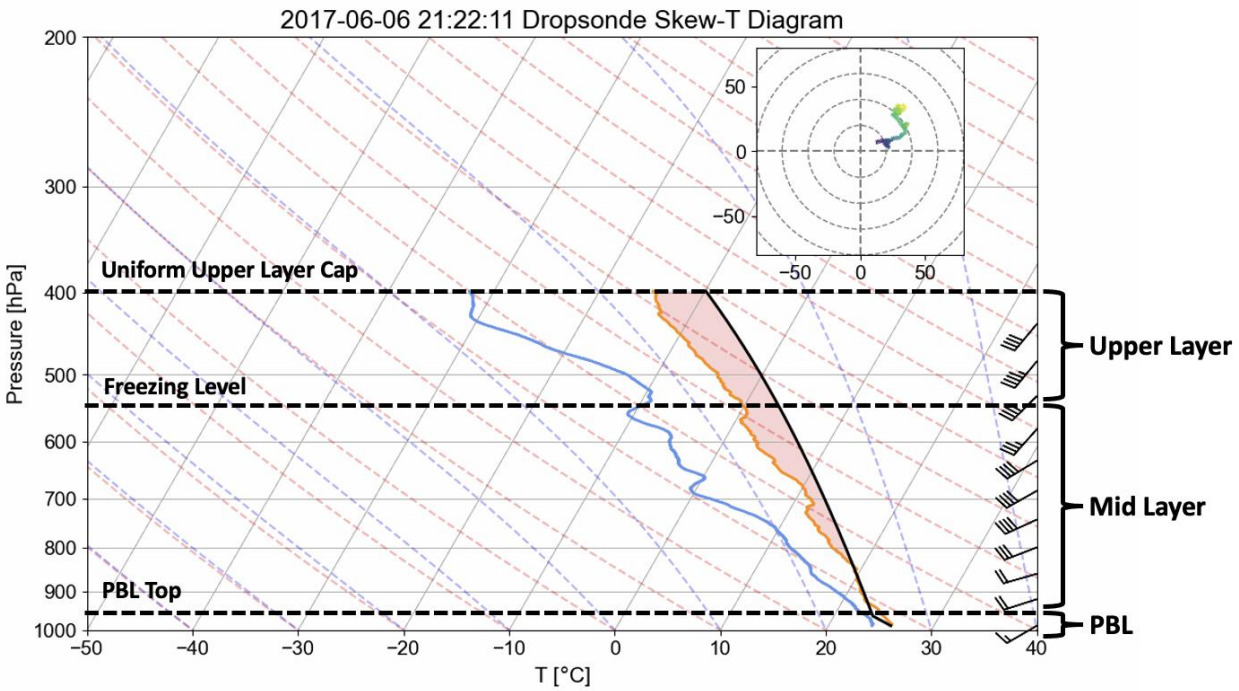

Figure 9: Skew-T diagram and hodograph for a Case 7 dropsonde (21:22:11 UTC) exemplifying the layer thresholds for which mean-layer RH and vertical speed shear are calculated. CAPE is shaded in light red, and wind barbs are provided on the right-hand side (full lines = 5 m s^{-1}, half lines = 2.5 m s^{-1}).

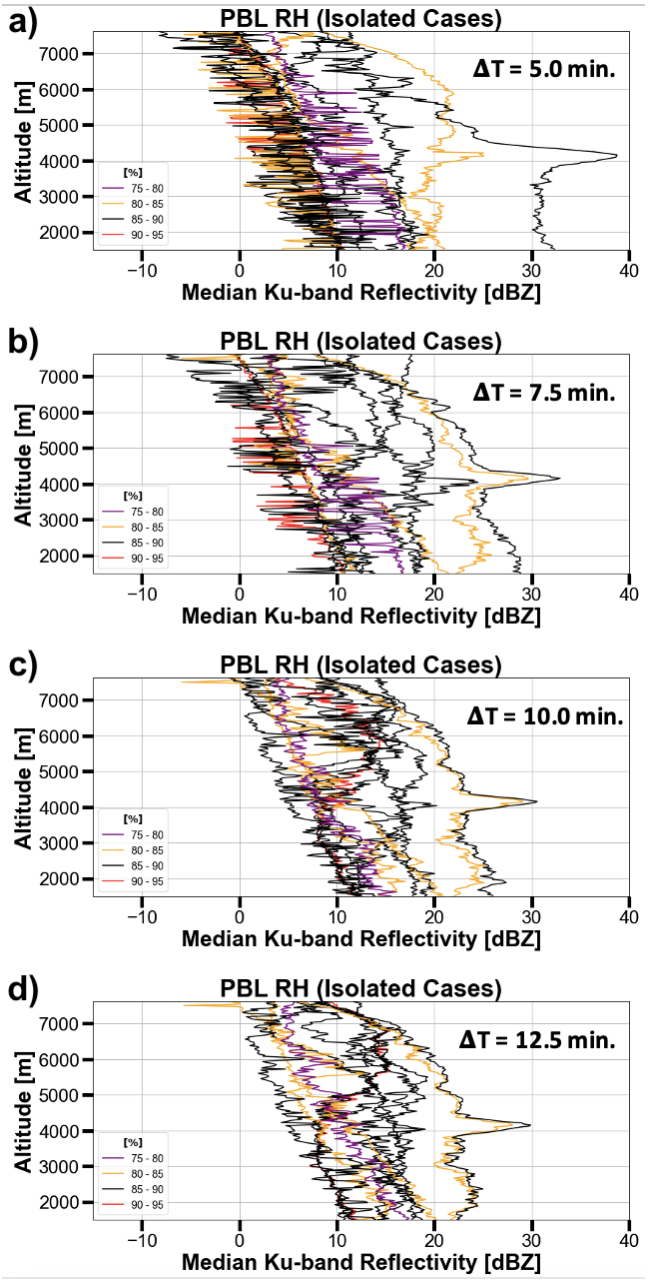

Figure 10: Median APR-3 Ku-band reflectivity profiles calculated for each dropsonde associated with an isolated case (In Precip dropsondes excluded) using a (a) 5.0-min, (b) 7.5-min, (c) 10.0-min, and (d) 12.5-min time delta. Profiles are color-coded by the PBL RH magnitude of the dropsonde they are associated with (5% bins).

Chapter 4

Results

a) Near-storm Environmental Relationships with Convective Type

To analyze potential near-storm environmental relationships with TOC type (i.e., isolated versus organized), mean-layer dropsonde metrics are presented as box-and-whisker plots (e.g., Figure 11a). Excluding the questionable In Precip dropsondes (i.e., owing to moisture biases), similar median PBL depths are observed for both convective types, while the upper and lower PBL depth quartiles are deeper (i.e., lower pressures) for organized convection (Figure 11a). Figure 11b reveals large PBL depth variability within each case (even when excluding In Precip dropsondes), with cases 4 and 16 primarily influencing the deeper upper quartile of organized convection PBL depth seen in Figure 11a. Owing to this variability, Figure 11b shows no clear relationship between PBL depth and convective type in the CPEX(-AW) region. *Large intra-case variability may partly be attributed to collection duration and varying distances of observations from the convection. However, spatial and temporal coverages of the observations cannot fully explain the large variability for PBL depth nor for the other upcoming metrics, as some cases have large metric variabilities despite convective flight legs covering small areas (e.g., Case 1 and Case 15) and/or having small observation periods (e.g., Case 15).*

Continuing to exclude In Precip dropsondes, isolated convection is observed to have greater median deep layer MUCAPE (929 J kg^{-1} vs. 900 J kg^{-1}, Figure 12a) and MLCAPE (570 J kg^{-1} vs. 524 J kg^{-1}, Figure 12b). More distinctly, isolated convection is also observed to have greater

median upper layer MUCAPE (613 J kg^{-1} vs. 549 J kg^{-1}, Figure 12c) and MLCAPE (393 J kg^{-1} vs. 317 J kg^{-1}, Figure 12d) compared to organized convection. Similar to PBL depth, large CAPE variability exists within each convective type, motivating further observational grouping by case (Figure 13). The further detail provided by the case grouping points to no clear relationship between convective type and MUCAPE/MLCAPE in either layer. However, some cases—even of similar convective type—do have distinctly different CAPE magnitudes compared to others (e.g., isolated cases 1 and 3 with upper layer CAPE), which will be investigated more in Section 4c and Section 4d.

Figure 14, again excluding In Precip dropsondes, reveals organized convection to be associated with slightly greater median RH in the PBL (88.8% vs. 85.8%, Figure 14b) and upper layer (55.6% vs. 53.0%, Figure 14d), while isolated convection is associated with a slightly greater median deep layer RH (66.1% vs. 64.5%, Figure 14a). Both isolated and organized convection have similar mid layer median RH (71.0% vs. 71.7%, Figure 14c), which regionally differs from aforementioned western Pacific studies that consistently link greater mid layer RH to more organized convection. As with PBL depth and CAPE, large mean-layer RH spreads exist for both convective types, particularly for organized convection. Further grouping the dropsonde observations by case highlights large mean-layer RH variability within many cases, especially cases 1, 13, and 16 (Figure 15). Cases 13 and 16, in particular, record some of the lowest mean-layer RH values of any case and will be investigated further in Section 4e. When comparing the clear air dropsondes for each case across convective type, deep layer RH is generally greater for isolated convection (Figure 15a), while PBL RH is generally greater for organized convection (Figure 15b). Distinct

mean-layer RH differences between cases of similar convective type do exist, however, and further motivate the case comparisons in Section 4c and Section 4d.

Organized convection is observed to have greater median PBL (5.0 kts vs. 3.5 kts, Figure 16b), mid (17.7 kts vs. 8.6 kts, Figure 16c), and deep layer (22.0 kts vs. 16.0 kts, Figure 16a) speed shears compared to isolated convection. As with prior metrics, a large degree of mean-layer speed shear variability exists within each convective type (especially for organized convection), motivating further dropsonde grouping by case (Figure 17). Large speed shear spreads are evident for each layer for each case and are notably unrelated to the environment the dropsondes were deployed into (i.e., Clear, In Cloud, or In Precip). Similar to CAPE and RH, distinct mean-layer speed shear differences do exist amongst cases of similar convective type, which further warrants comparing individual cases in Section 4c and Section 4d. Ultimately though, organized convection is associated with generally greater PBL, mid, and deep layer near-storm speed shear than isolated convection (Figure 17a,b,c).

Incorporating the spatially and temporally denser DAWN observations provides an enhanced look into deep layer speed shear trends (Figure 18). The addition of the DAWN observations reveals even larger deep layer speed shear variability within each convective type (Figure 18a) and each convective case (Figure 18c) than the dropsonde observations previously showed. Separating the convective cases by field campaign (Figure 18b, see also Table 1) uncovers differing deep layer speed shear spreads for the three CPEX isolated cases compared to the one CPEX-AW isolated case, though the deep layer shear spreads for the six CPEX and two CPEX-AW organized cases are similar. Factoring in DAWN, median deep layer speed shear is actually greater for isolated

convection compared to organized convection (25.0 kts vs. 21.2 kts, Figure 18a), which the less frequent dropsonde data did not capture. This result is highly influenced by Case 15 from CPEX-AW, which recorded some of the greatest deep layer shear values in either campaign, exceeding 45 knots (Figure 18c). When comparing all isolated case speed shear observations with the organized cases, however, the relationship between deep layer speed shear and convective type is unclear (Figure 18c).

Overall, the composite analysis of near-storm environmental relationships with convective type reveals broad near-storm environmental metric variability within each convective type. However, general mean-layer CAPE, RH, and speed shear trends do exist with regards to two-dimensional (2-D) TOC structure. As such, it raises the question whether similar (or perhaps even more pronounced) near-storm environmental trends apply to vertical convective structure (i.e., convective intensity) for each convective type.

b) Near-storm Environmental Relationships with Convective Intensity (Composite Analysis)

Median Ku-band reflectivity profiles in combination with associated dropsonde metrics were used to analyze composite near-storm environmental relationships with convective intensity. Median Ku-band reflectivity profiles for each qualifying dropsonde (see Section 3d) were constructed, grouped by convective type, and color-coded by their respective dropsonde's mean-layer environmental metrics to discern possible environmental metric influence on vertical reflectivity (i.e., a proxy for hydrometeor size and convective intensity). Dropsondes lacking Ku-band reflectivity data within the utilized 10-minute time delta were omitted from this analysis. Alternate

time deltas were also tested (see Section 3d) and produced similar results to the 10-min time delta shown in subsequent figures.

The greatest reflectivities below 7 km (i.e., near the upper layer cap of 7622.5 m) for isolated convective cases, which exceed 20 dBZ, are associated with greater deep layer (600 – 800 J kg^{-1}) and upper layer (400 – 500 J kg^{-1}) MLCAPE, though the relationships are non-monotonic (Figure 19e,g). This relationship could result from enhanced thermodynamic instability promoting stronger updrafts, which can suspend hydrometeors for longer periods of time and support continued hydrometeor growth. However, the lack of parallel reflectivity relationships with MUCAPE casts doubt on this suggestion. For the organized cases, no clear mean-layer CAPE trends with vertical reflectivity profile strength exist (Figure 19b,d,f,h).

For the isolated convective dropsondes, the greatest reflectivities below 7 km are also associated with the greatest mid layer RH values (75% – 80%), though the relationship is non-monotonic (Figure 20e). This relationship could be due to enhanced hydrometeor growth and less negative buoyancy introduction from less dry air entrainment into the single-core systems. Similar to CAPE, no clear mean-layer RH trends with vertical reflectivity profile strength are apparent for organized convective cases (Figure 20b,d,f,h).

For isolated cases, the greatest reflectivities below 7 km are additionally associated with greater deep layer (20 – 30 kts) and mid layer (10 – 20 kts) speed shear (Figure 21a,e). The relationships remain non-monotonic but are more distinct than the aforementioned CAPE and RH trends. This relationship could result from more effective separation of the convective updraft and downdraft

in single-core systems by larger speed shear environments. For the organized cases, the greatest reflectivities below 7 km (exceeding 30 dBZ) are associated with generally lesser speed shears in each of the four layers (Figure 21b,d,f,h). The relationships are non-monotonic and contrast with the isolated convection speed shear relationships, which may point to differing dynamical relationships between single-core systems and multi-core systems with their near-storm environments.

Overall, there are no consistent (i.e., monotonic) CAPE, RH, nor speed shear trends with median vertical reflectivity profile strength both within and across convective type. However, while the median Ku-band reflectivity profile analysis explores large near-storm environmental metric variability within each convective type in the context of convective intensity, it does not distinguish observations by case and thus does not provide case by case comparisons. With the 2-D composite analysis in Section 4a revealing distinct metric differences (i.e., variability) between cases of similar convective type, a case comparison approach is warranted on how near-storm environments relate to convective intensity for each convective type.

c) Near-storm Environmental Relationships with Convective Intensity (Isolated Case Comparisons)

To compare convective intensities of isolated cases, normalized CFADs (see Section 3e) were created for each isolated case (except Case 15, which lacked APR-3 reflectivity data). Then, cases with distinctly different mean-layer metric values (omitting In Precip dropsondes from CAPE and RH analysis due to aforementioned moisture biases) had their normalized CFADs differenced to visually determine which case had more frequent greater Ku-band reflectivities throughout the

vertical column (i.e., which convective system was more intense). Subsequent comparison of convective intensities and their associated dropsonde mean-layer environmental metrics was performed. Ensuing CFAD figures were normalized by the maximum bin count in each height interval. However, similar analysis was performed with CFADs normalized by maximum bin count in any height interval, and each method produced the same conclusions.

Isolated cases 1 and 2 had many distinct metric differences that motivated convective intensity comparison. Case 1 had notably greater PBL RH than Case 2, but lesser average deep layer RH (Figure 15a,b). Case 1 also had greater average deep layer, PBL, and upper layer speed shear (Figure 17b,d; Figure 18c). Additionally, Case 1 had distinctly greater deep layer and upper layer MUCAPE and MLCAPE compared to Case 2 (Figure 13). When comparing the normalized CFADs of the two cases, Case 1 was ultimately the more intense isolated convection (Figure 22). Figure 23 illustrates the difference CFAD between Case 1 and Case 3. Case 1 was the more intense convection and, while having similar mean-layer RH and speed shear to Case 3, it was associated with notably larger upper layer MUCAPE, upper layer MLCAPE, and deep layer MLCAPE (Figure 13b,c,d). When comparing Case 2 and Case 3, Case 3 had distinctly greater upper layer RH, upper layer speed shear, and PBL speed shear, along with greater deep and upper layer MUCAPE (Figure 15d; Figure 17b,d; Figure 13a,c). With cases 2 and 3 each possessing greater Ku-band reflectivity frequencies at certain height levels (Figure 24), it is unclear which case was the more intense convection. Together, these three case comparisons show the more intense isolated case throughout the vertical column (i.e., Case 1) to consistently possess greater upper layer MUCAPE and MLCAPE and greater deep layer MLCAPE. Similar to a postulation in

Section 4b, this relationship could result from greater CAPE environments promoting hydrometeor growth through enhanced thermodynamic instability (i.e., buoyancy).

d) Near-storm Environmental Relationships with Convective Intensity (Organized Case Comparisons)

Convective intensity comparisons between organized cases were executed with methods similar to that of the isolated case comparisons. Likewise, the subsequent CFAD figures were normalized by the maximum bin count in each height interval, and their results are consistent with the alternative normalization method. It should be noted that Case 7 had the lowest aircraft flight height (~7.0 – 7.5 km) amongst all the analyzed convective cases. Therefore, ensuing visual inspection of difference CFADs (all involving Case 7) should disregard reflectivity frequency differences above 7 km.

For organized convection, distinct metric differences between cases were predominantly with mean-layer speed shear. When comparing Case 7 and Case 16, Case 16 had notably lesser mid layer speed shear (Figure 17c) and was the more intense convection (Figure 25). Meanwhile, Case 13 had distinctly lesser mid layer speed shear compared to Case 7 (Figure 17c) and was less intense than Case 7 (Figure 26). Case 7 and Case 8 had many distinct metric differences that motivated convective intensity comparison. Case 8 was the more intense convection (Figure 27) with notably lesser mid layer speed shear, but notably greater PBL speed shear, upper layer RH, and deep layer MUCAPE (Figure 17b,c, Figure 15d, Figure 13a). Comparing Case 7 to Case 5, Case 5 had typically lesser deep layer and mid layer speed shear (Figure 18c, Figure 17c) and was the more intense convection (Figure 28). Meanwhile, Case 7 had typically greater deep layer speed shear

compared to Case 4 (Figure 18c), along with lesser PBL speed shear and greater PBL RH (Figure 17b, Figure 15b). Differencing Case 7 and Case 4 Ku-band reflectivity frequencies revealed Case 7 to be more intense than Case 4 (Figure 29). Lastly, when comparing Case 7 and Case 14 (Figure 30), the more intense Case 14 generally had lesser deep layer and mid layer speed shear, but notably greater deep layer and upper layer RH (Figure 18c, Figure 17c, Figure 15a,d).

In total, when comparing CPEX(-AW) organized convective cases with distinct mean-layer environmental metric differences, no consistent mean-layer speed shear, MUCAPE, nor MLCAPE relationships with convective intensity are found. However, when a notable difference in upper layer RH existed between two organized cases, the more intense convection was consistently associated with greater upper layer RH. Similar to a postulation in Section 4b, this relationship could be due to less dry air entrainment promoting enhanced hydrometeor growth and limiting negative buoyancy introduction. When intercomparing the isolated case comparison results with the organized case comparison results, it is noteworthy that there are no similar, consistent near-storm mean-layer metric trends with convective intensity. This lack of similarity between convective types further supports a notion from Section 4b that single-core and multi-core systems interact differently with their near-storm environments. An additional lack of consistent near-storm environmental relationships with organized TOC intensity suggests multi-core systems also variably interact with their near-storm environments. The latter finding is likely attributed to diverse vertical organizational structures of multi-core TOC, which were observed during CPEX(-AW) and will be explored further in the following section.

e) Case 13 vs. Case 16 Organized Convection Analysis

As highlighted in Section 4a, large mean-layer RH variability existed within each sampled convective system, but especially within Case 13 and Case 16. Upon further examination, cases 13 and 16 containing many of the lowest mean-layer RH values of any sampled CPEX(-AW) convective system was responsible for their particularly large RH spreads (Figure 15). The relatively dry near-storm observations, coupled with the especially large RH variability, motivated further investigation into these two cases' convective environments.

The convective flight legs and observations of cases 13 and 16 each encompassed a synoptic-scale horizontal moisture gradient (Figure 31), providing the reason for large intra-case RH spreads and notably dry near-storm observations that were particularly influential on the RH results of Section 4a. No other observed convective systems during CPEX(-AW) were located near synoptic-scale moisture gradients, making Case 13 and Case 16 unique in that aspect. Further exploring the two cases, both had similar 2-D structures (Figure 31) with an intensifying sector (e.g., Figure 32) and a matured sector (e.g., Figure 33) identified by decreasing and increasing infrared brightness temperatures with time, respectively. Both cases were similarly located on the moist side of their respective synoptic-scale moisture gradient, with each moisture gradient collocated with a similar strength (~15 m s^{-1}), along-gradient 800 – 650 mb mid-level jet (Figure 34). However, despite similar 2-D structures and synoptic-scale environmental features, the vertical structures of the organized Case 13 and Case 16 convective systems were markedly different. Case 13 was mainly composed of leading line convective elements with trailing stratiform (Figure 35), while Case 16 was mainly composed of numerous embedded convective elements within predominant widespread stratiform (Figure 36). With the differing vertical convective structures of otherwise

similar convective systems with similar synoptic-scale environments, cases 13 and 16 provided a unique opportunity to investigate how differing organized vertical convective structures relate to near-storm moisture and speed shear.

In addition to aforementioned dropsonde characterizations in Section 3b, all dropsonde and DAWN observations for the Case 13 and Case 16 analysis were contextualized as being collected within or beyond each case's synoptic-scale moisture (TPW) gradient. No clear relationship was found between mean-layer speed shear and location of observations relative to the moisture gradient. As such, mean-layer speed shear comparisons were made across all observations, with the result of Case 13 and Case 16 having similar mean-layer speed shear (Figure 37). It is notable that PBL shear within the moisture gradient was distinctly greater for Case 13 (4.1 – 8.7 kts) compared to Case 16 (0.4 – 2.7 kts) (Figure 37b). This greater PBL shear could explain Case 13 being more linearly organized than Case 16, consistent with studies of linearly organized TOC and low-level shear in the western Pacific basin (Alexander and Young, 1992; LeMone et al., 1998; Chudler and Rutledge, 2021). However, all the Case 16 PBL shear observations within the moisture gradient were collected in actively precipitating regions, which may have been influenced by cold pools and thus not directly comparable to the Case 13 observations in non-precipitating regions.

Observations collected within the moisture gradient unsurprisingly tended to have greater mean-layer RH compared to observations collected beyond the moisture gradient (Figure 38). With Case 16 only having quality (i.e., not In Precip) RH observations beyond the moisture gradient, mean-layer RH comparisons were only performed amongst data collected from the impinging dry air

beyond the moisture gradient associated with each convective system. The deep layer and mid layer were notably drier for Case 16 compared to Case 13 (Figure 38a,c), with the 800 – 650 mb jet layer (located entirely within the mid layer) in particular having dewpoint depressions exceeding three times those of Case 13 (Figure 34). The distinctly differing near-storm environmental moisture of cases 13 and 16 motivated further analysis on how the near-storm environments may have influenced convective intensity.

When analyzing both case's convective intensities in relation to near-storm environmental metrics using CFADs, Case 16 had the more intense intensifying sector (Figure 39) with lesser average mid layer RH and lesser average deep layer, PBL, and upper layer speed shear. Case 16 also had the more intense matured sector (Figure 40), but with similar mean-layer RH and speed shear to the Case 13 matured sector. All four sectors (i.e., intensifying and matured for both cases) and their associated mean-layer environmental metrics were also compared and ranked against one another. The Case 16 embedded convection had the two most intense sectors overall, yet it had similar mean-layer speed shear to the two less intense sectors (i.e., the Case 13 sectors). However, the Case 16 sectors had the two lowest average deep layer and mid layer RHs and the two highest average upper layer RHs.

Ultimately, Case 16 was more intense than Case 13 despite similar near-storm, mean-layer speed shear and distinctly drier impinging air in the deep layer and mid layer. However, dropsonde observations from the northern and southern halves of Case 16 reveal the presence of synoptic-scale low-level convergence (Figure 41), which was not observed in Case 13. This broad low-level convergence was likely the reason for Case 16 being notably more intense than Case 13, despite

much drier impinging air. Overall, the Case 13 and Case 16 analysis suggests that sufficient large-scale low-level convergence can provide enough forcing for TOC to thrive in otherwise seemingly less favorable near-storm environmental conditions, and it may also influence the vertical structure of organized convection (e.g., increasing the number and intensity of convective elements).

f) Figures

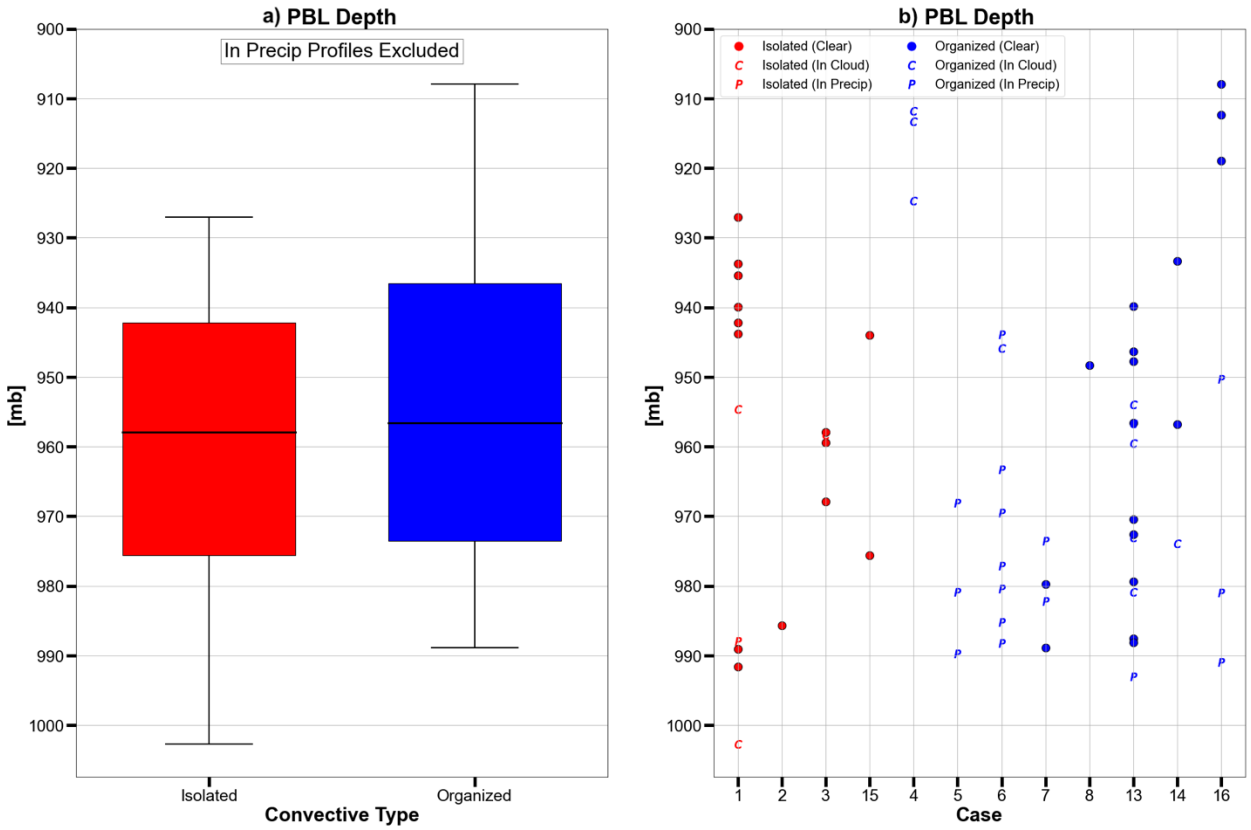

Figure 11: (a) Dropsonde-derived PBL depth for isolated (red) and organized (blue) TOC systems sampled during CPEX and CPEX-AW (In Precip profiles excluded). Each box extends from the first quartile to the third quartile of the data, with a black line at the median. Whiskers extend from the box by up to 1.5 times the inter-quartile range. (b) Same data as (a), but dropsonde observations are further sorted by convective case (In Precip profiles included as well). Markers denote the convective-relative environment the dropsonde was deployed into.

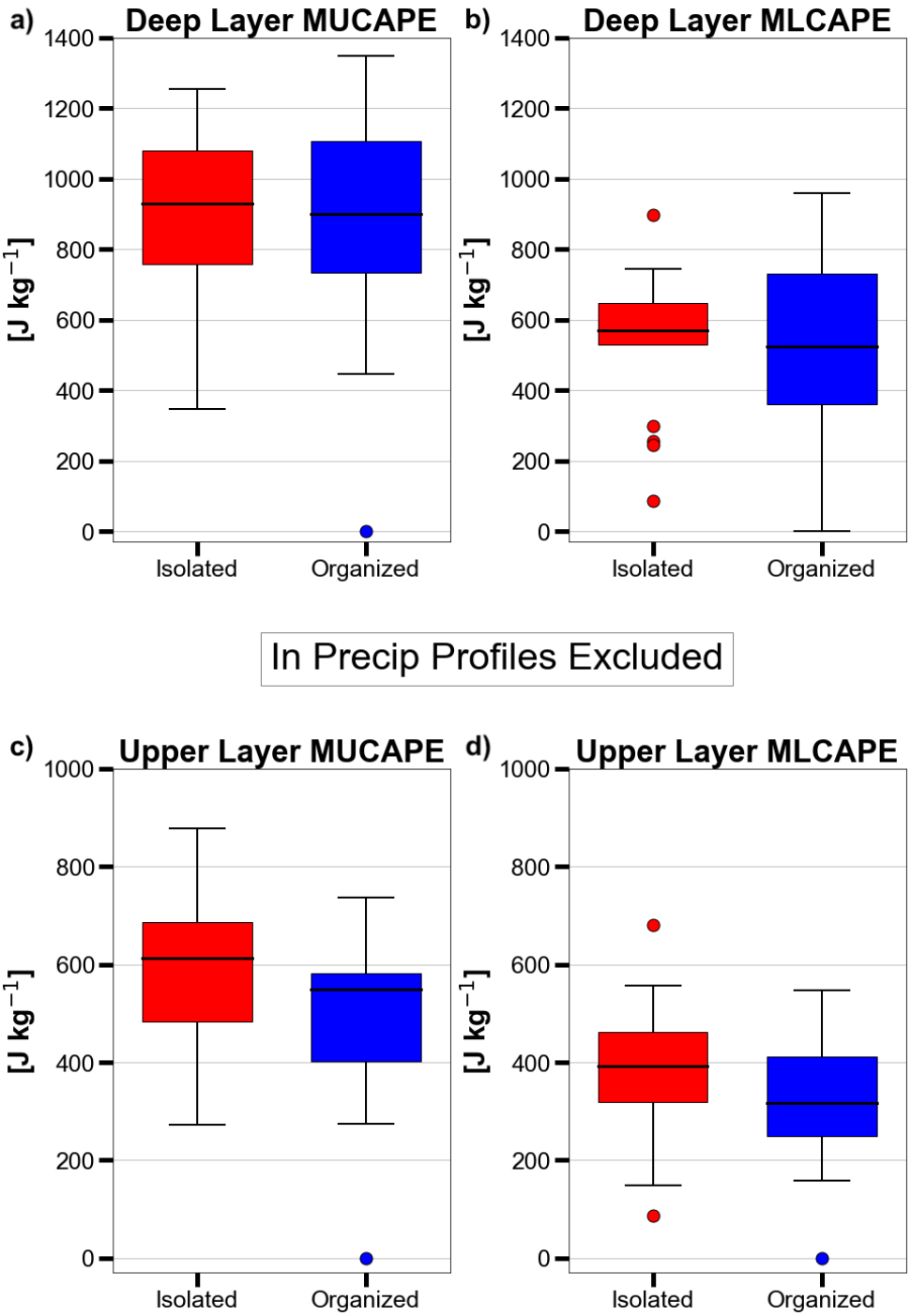

Figure 12: Same as Figure 11a, except showing (a) deep layer MUCAPE, (b) deep layer MLCAPE, (c) upper layer MUCAPE, and (d) upper layer MLCAPE. Flier points are points beyond the whiskers.

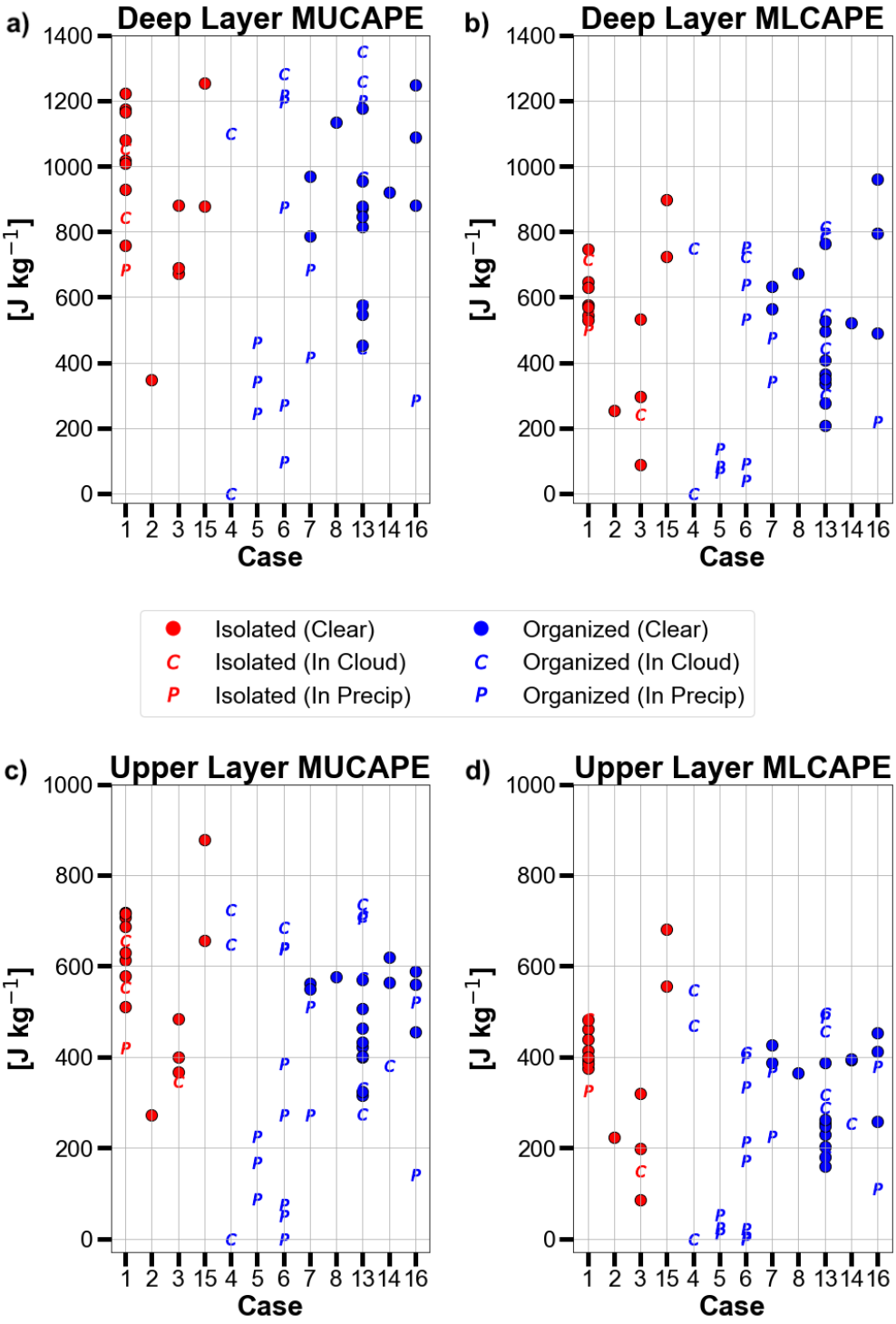

Figure 13: Same data as Figure 12, but dropsonde observations are further sorted by convective case (In Precip profiles included as well). Markers denote the convective-relative environment the dropsonde was deployed into.

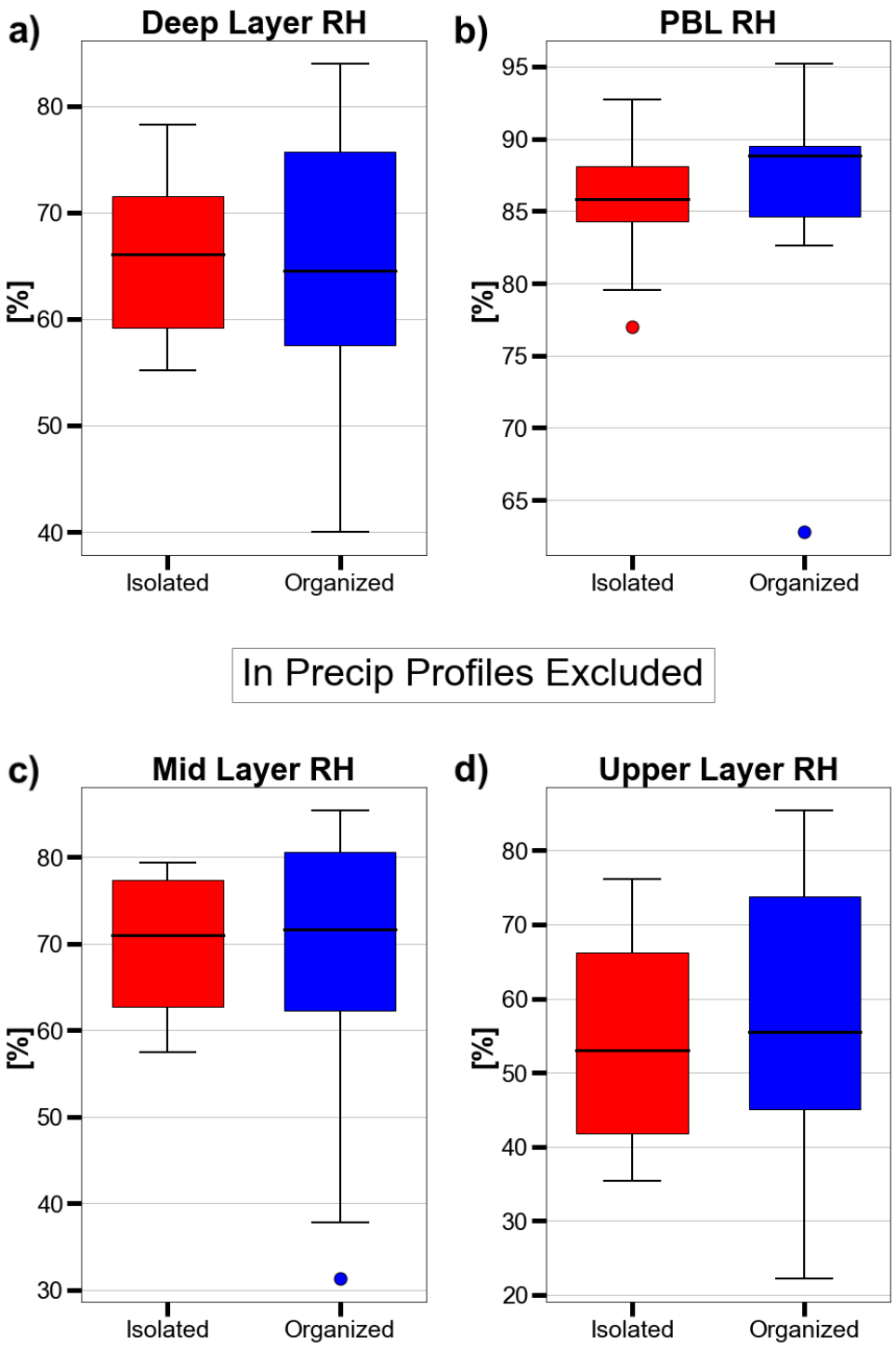

Figure 14: Same as Figure 12, except showing (a) deep layer RH, (b) PBL RH, (c) mid layer RH, and (d) upper layer RH.

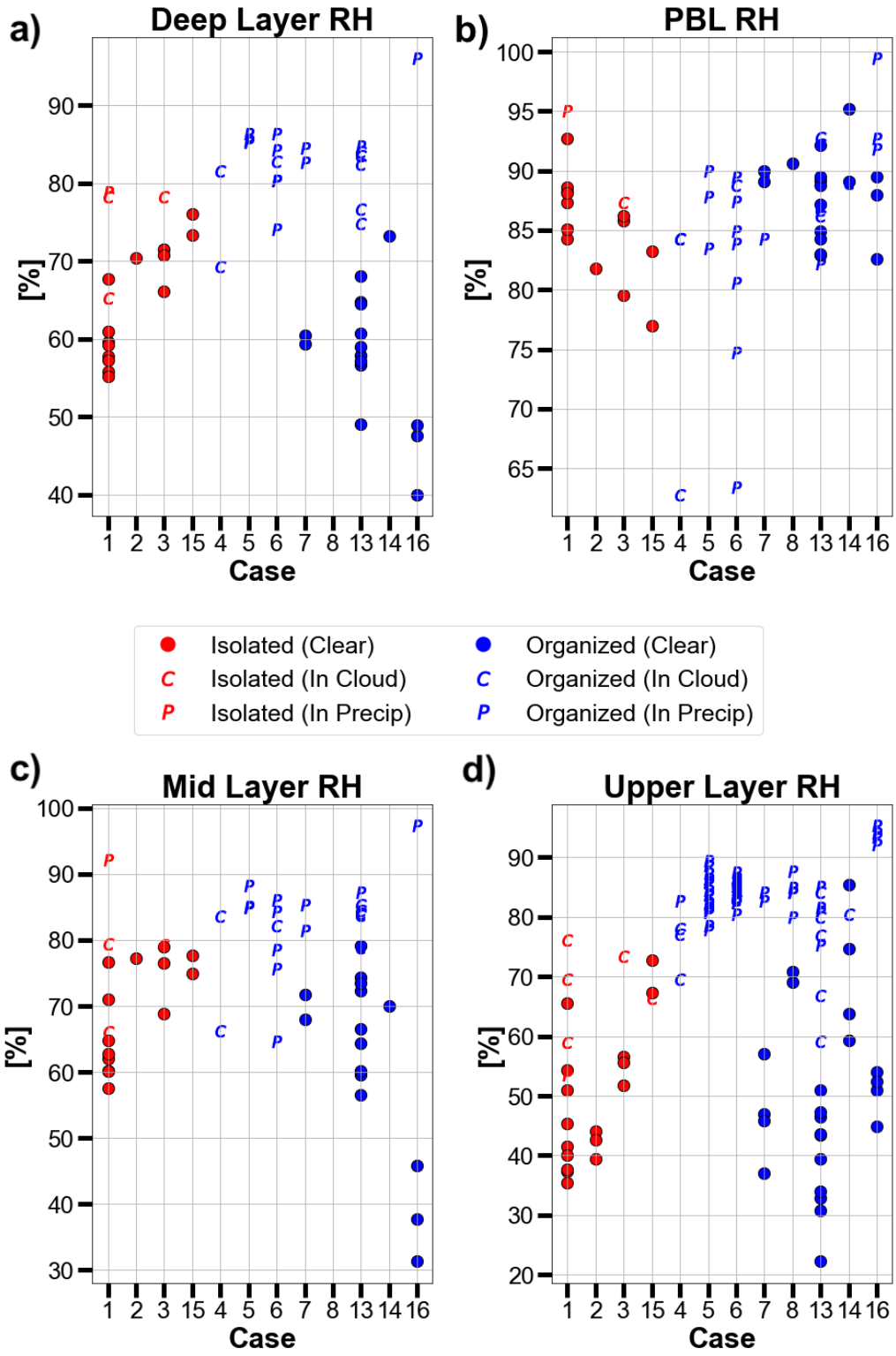

Figure 15: Same data as Figure 14, but dropsonde observations are further sorted by convective case (In Precip profiles included as well). Markers denote the convective-relative environment the dropsonde was deployed into.

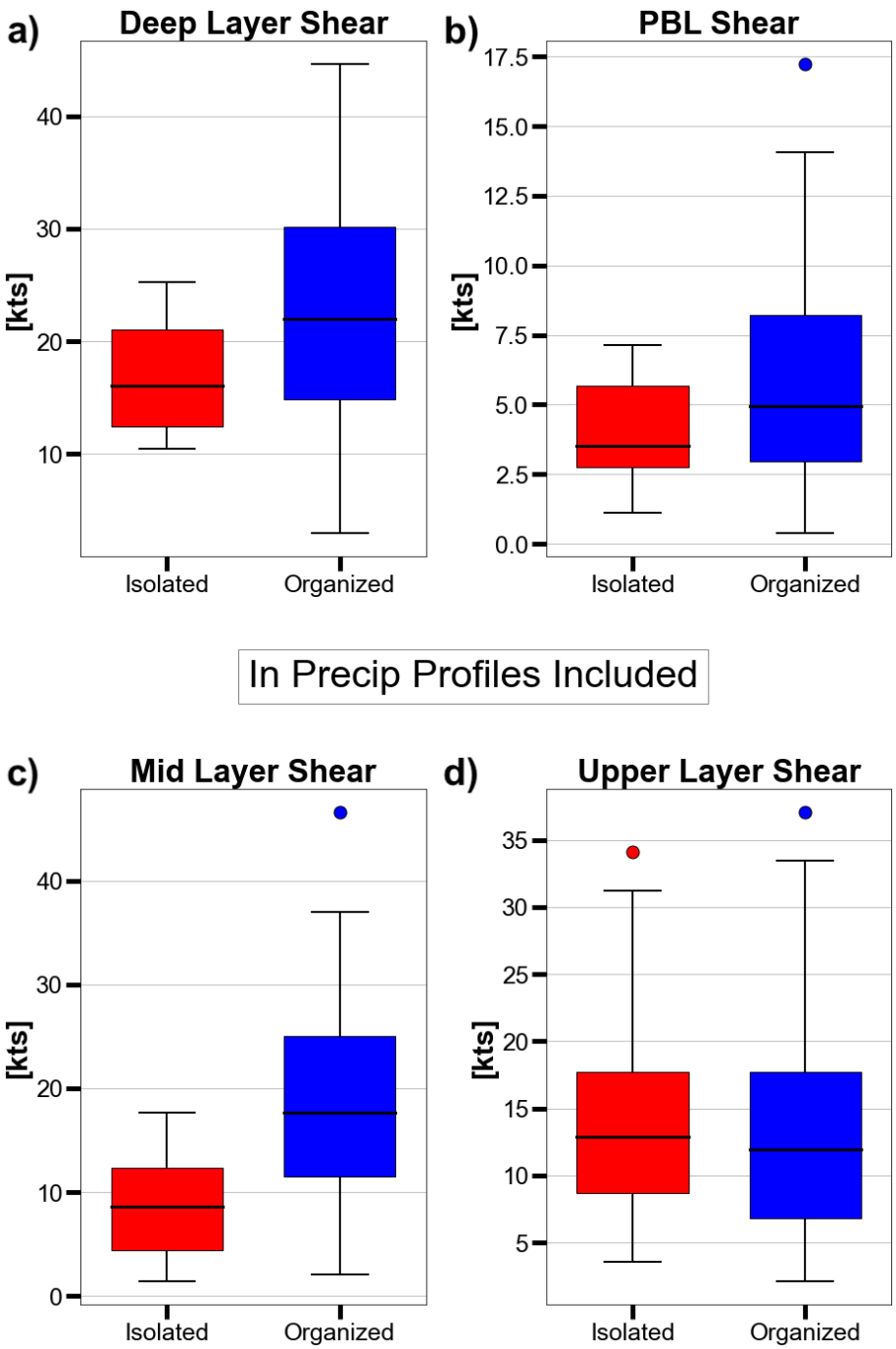

Figure 16: Same as Figure 12, except showing (a) deep layer speed shear, (b) PBL speed shear, (c) mid layer speed shear, and (d) upper layer speed shear. In Precip profiles are now included.

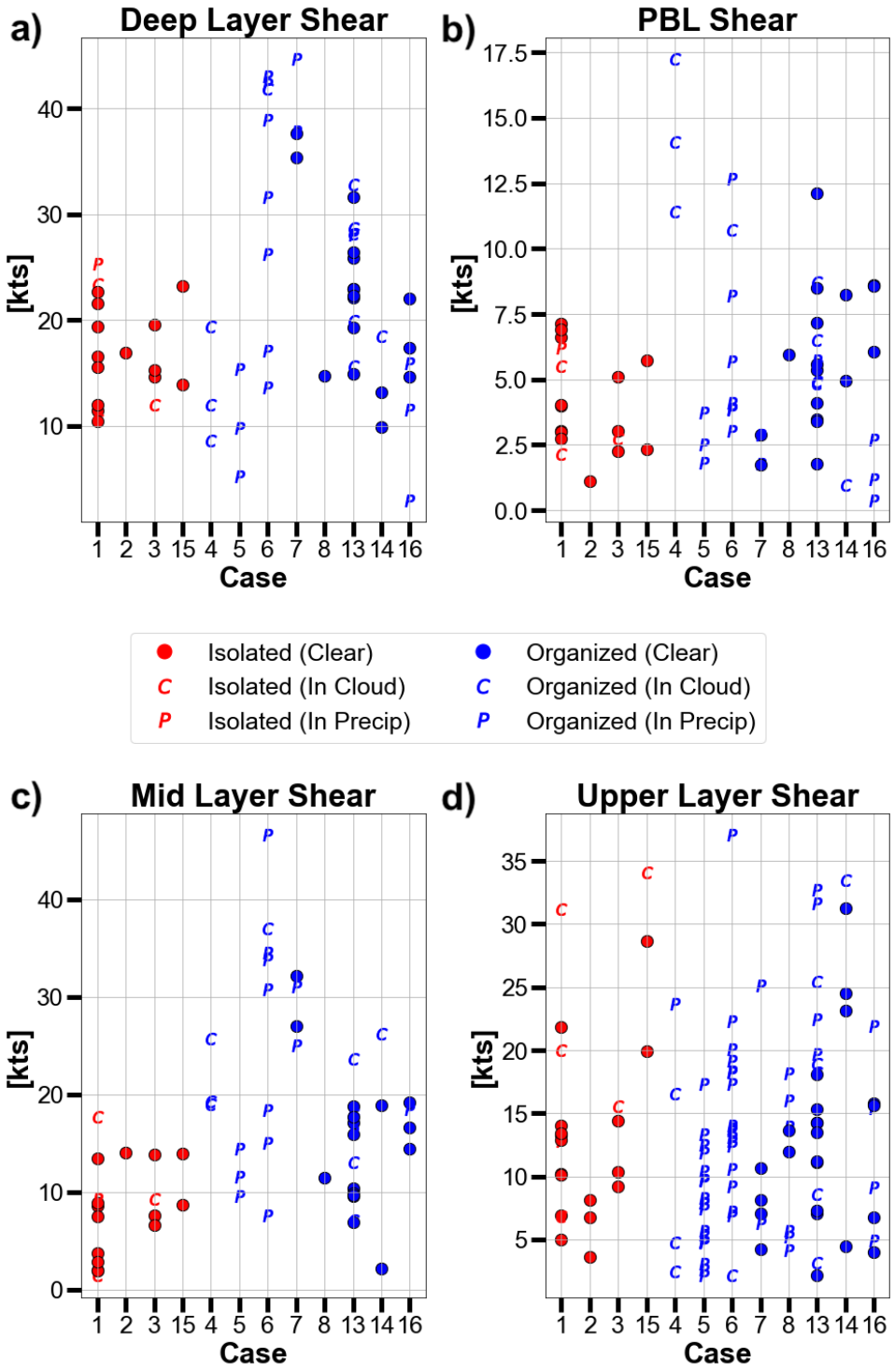

Figure 17: Same data as Figure 16, but dropsonde observations are further sorted by convective case. Markers denote the convective-relative environment the dropsonde was deployed into.

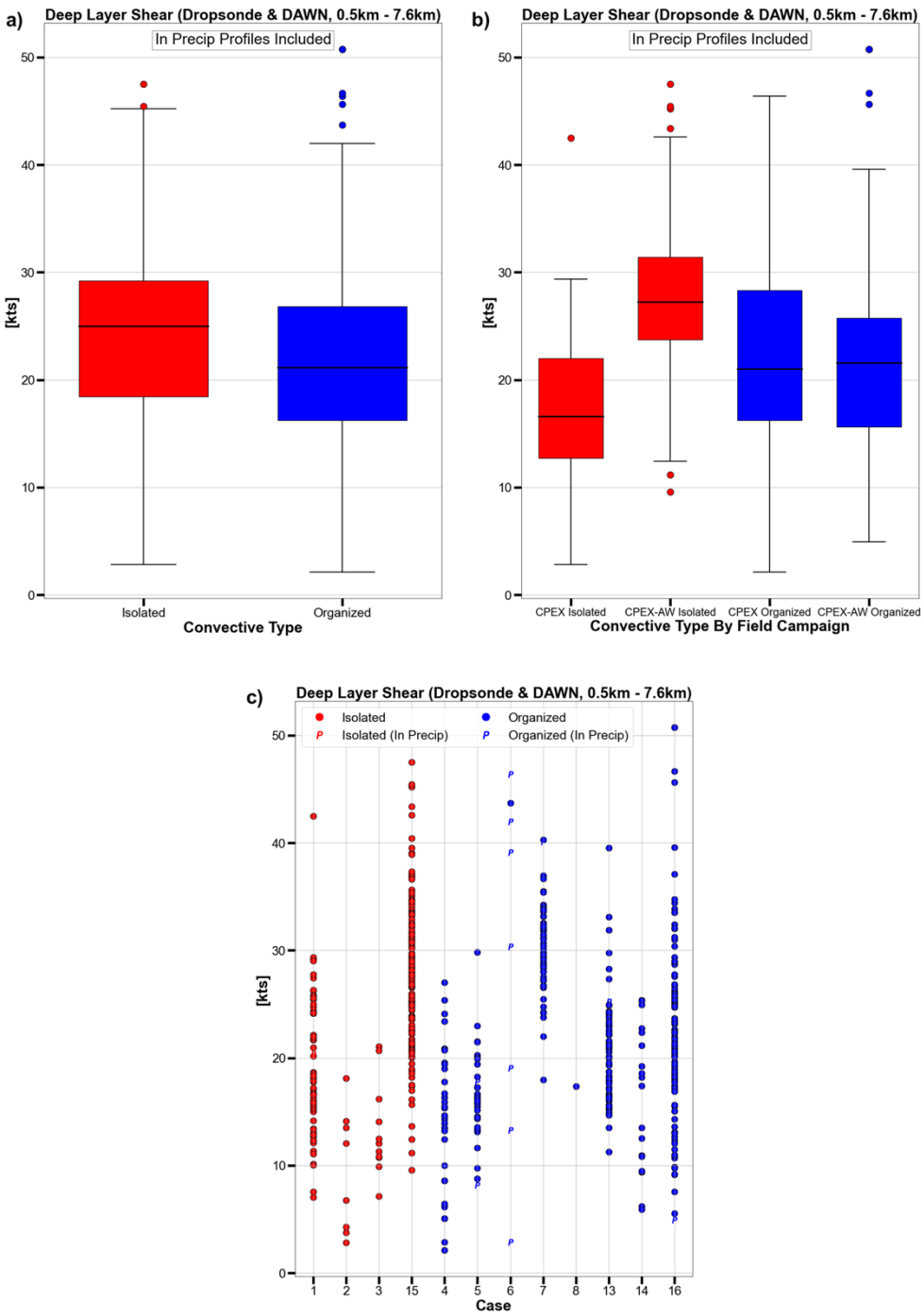

Figure 18: (a) Same as Figure 16a, except showing dropsonde- and DAWN-derived 0.5-km – 7.6-km deep layer speed shear. (b) Same as (a), but observations are further sorted by the field campaign they were collected from. (c) Same as (a), but observations are further sorted by convective case. Markers denote whether an observation was collected within an actively precipitating environment or not.

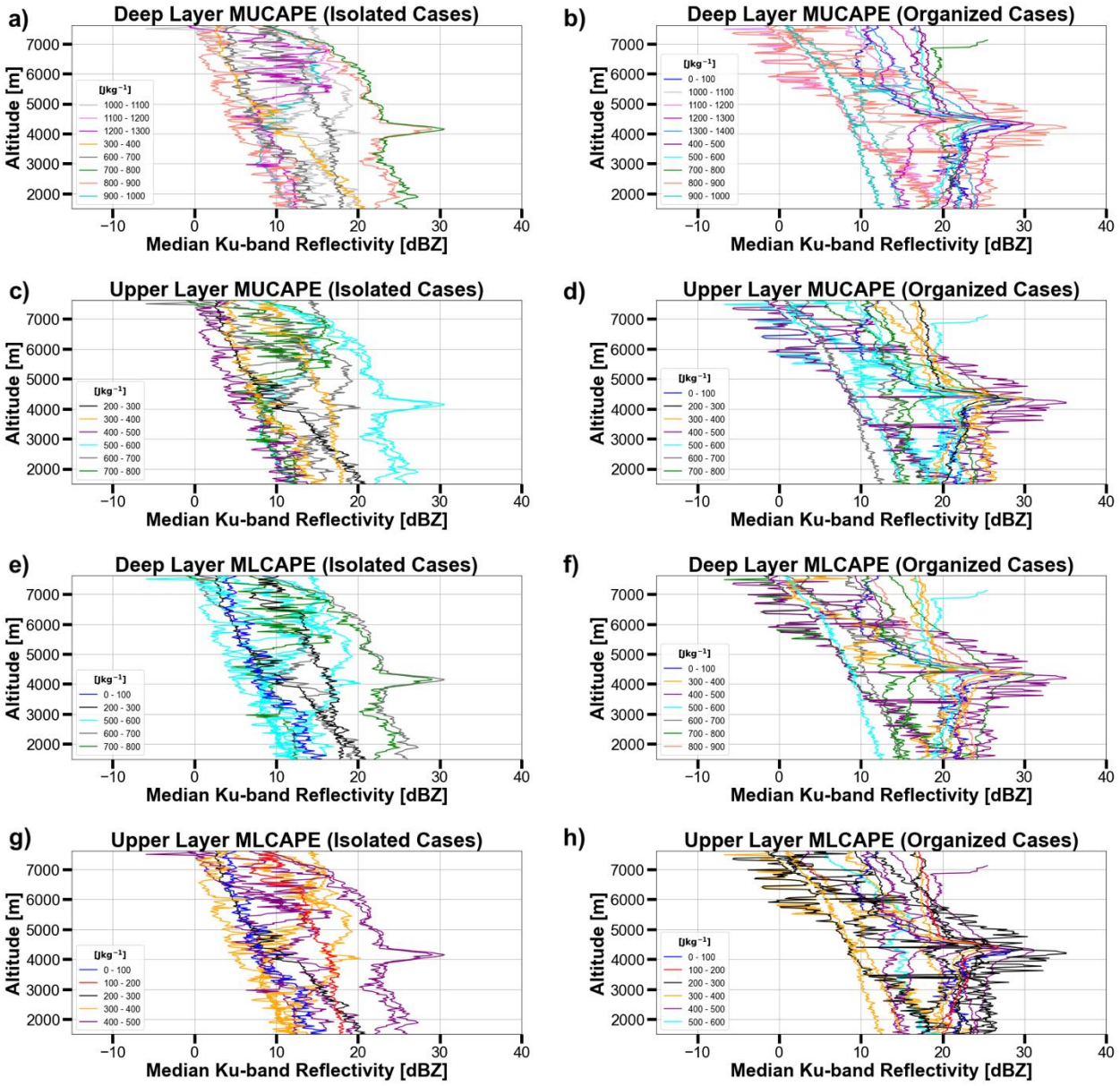

Figure 19: Median APR-3 Ku-band reflectivity profiles calculated for each dropsonde using a 10-min time delta (In Precip dropsondes excluded). Profiles are sorted by the convective type of the case they were associated with (left: isolated, right: organized). Profiles are color-coded by their associated dropsonde's (a,b) deep layer MUCAPE, (c,d) upper layer MUCAPE, (e,f) deep layer MLCAPE, and (g,h) upper layer MLCAPE magnitude (100 J kg^{-1} bins).

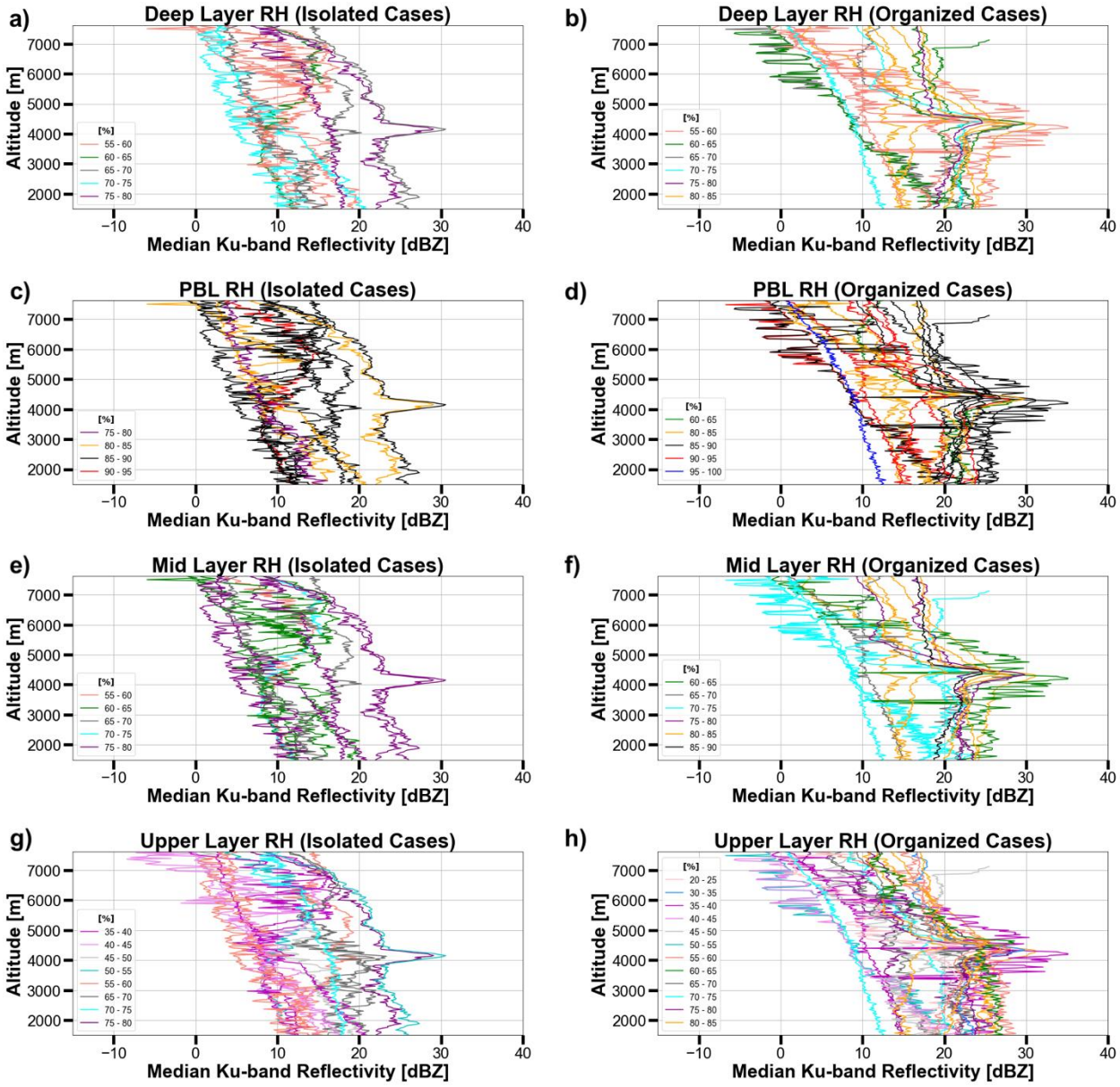

Figure 20: Same as Figure 19, but median APR-3 Ku-band reflectivity profiles are color-coded by their associated dropsonde's mean (a,b) deep layer RH, (c,d) PBL RH, (e,f) mid layer RH, and (g,h) upper layer RH magnitude (5% bins).

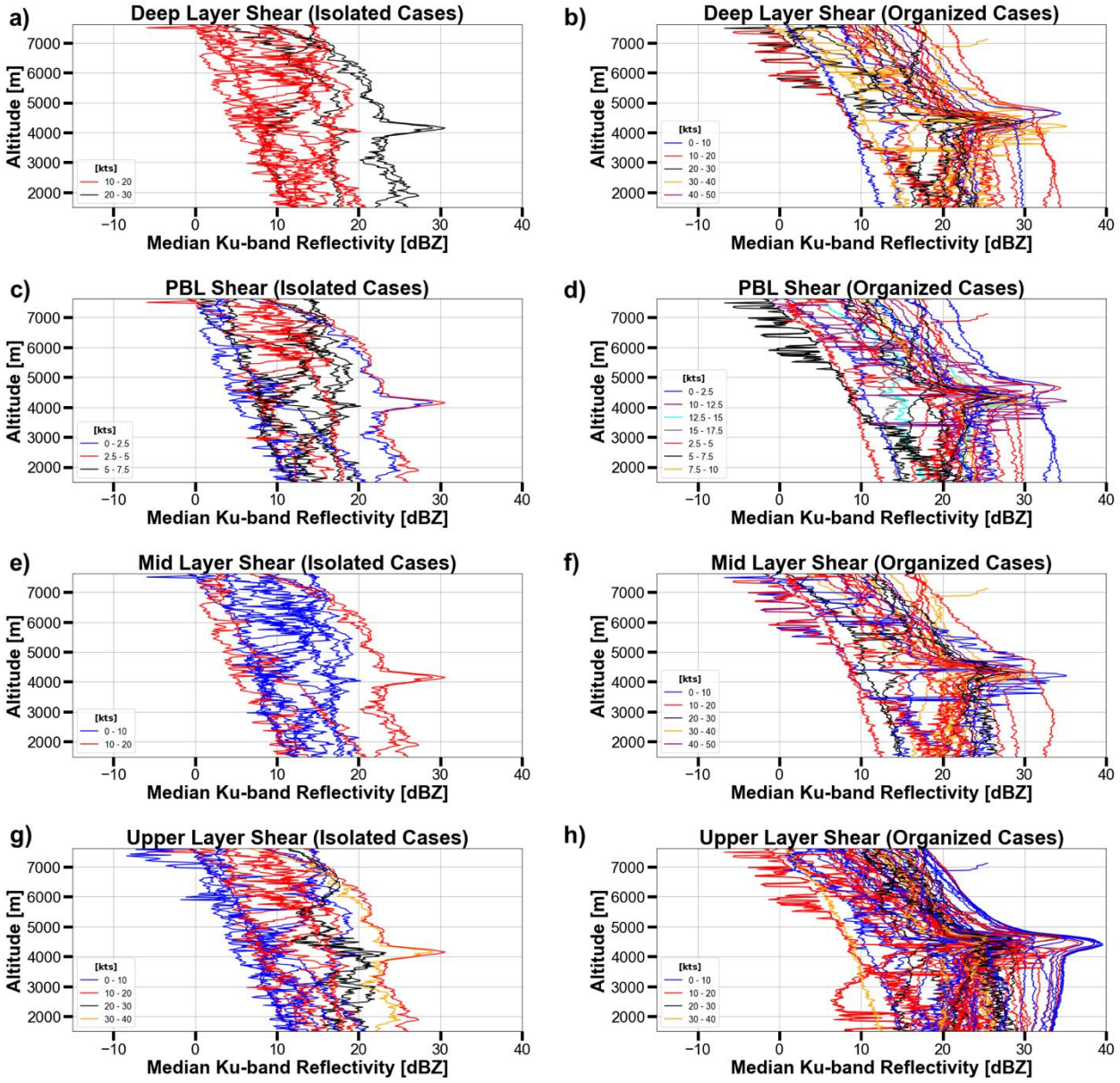

Figure 21: Same as Figure 19, but In Precip dropsondes are now included, and median APR-3 Ku-band reflectivity profiles are color-coded by their associated dropsonde's (a,b) deep layer speed shear, (c,d) PBL speed shear, (e,f) mid layer speed shear, and (g,h) upper layer speed shear magnitude (10 kt bins, except for PBL shear, which has 2.5 kt bins).

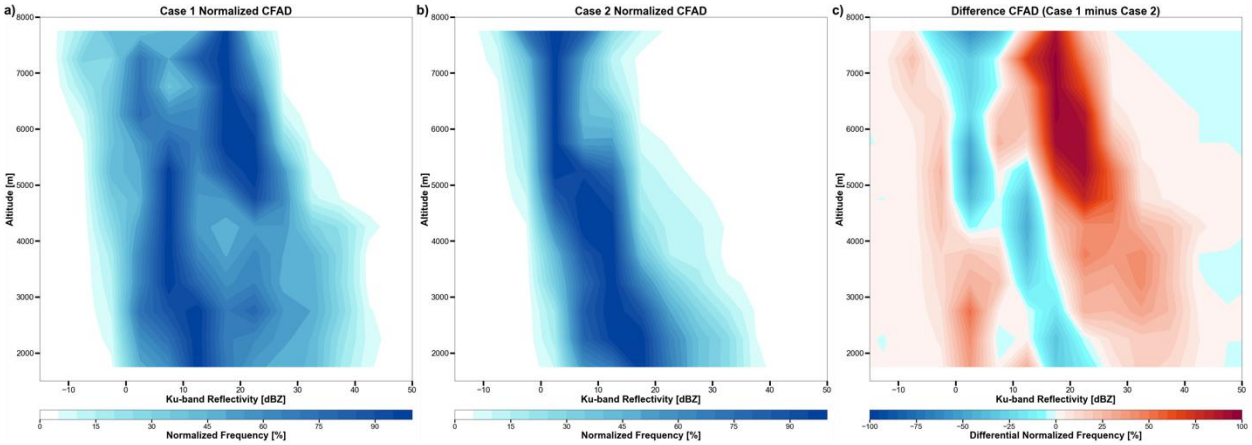

Figure 22: (a) Normalized CFAD of APR-3 Ku-band reflectivity for Case 1. Reflectivity data is binned into 5-dBZ and 0.5-km intervals and normalized by the maximum bin count in each height interval. (b) Same as (a) but for Case 2. (c) The Case 2 CFAD in (b) subtracted from the Case 1 CFAD in (a).

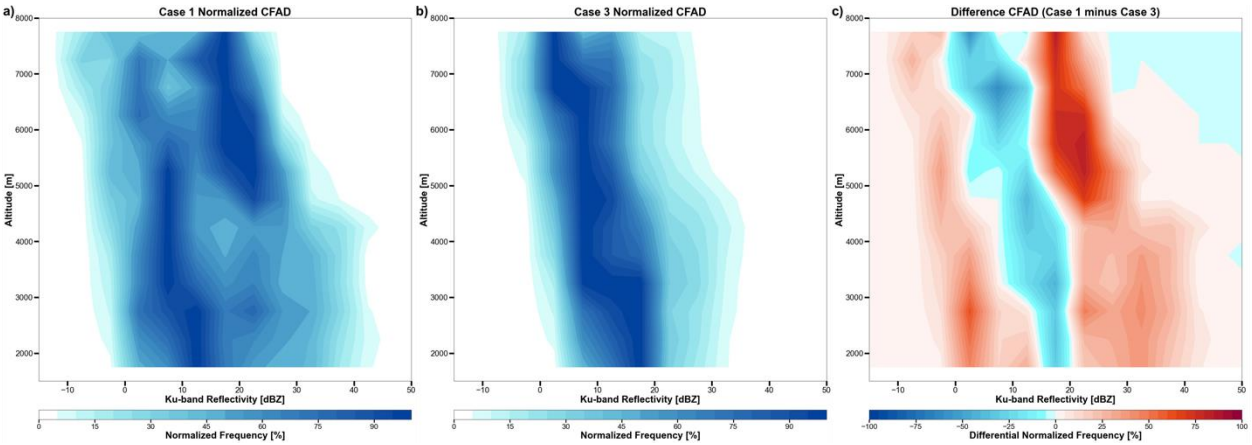

Figure 23: Same as Figure 22, but for Case 1 and Case 3.

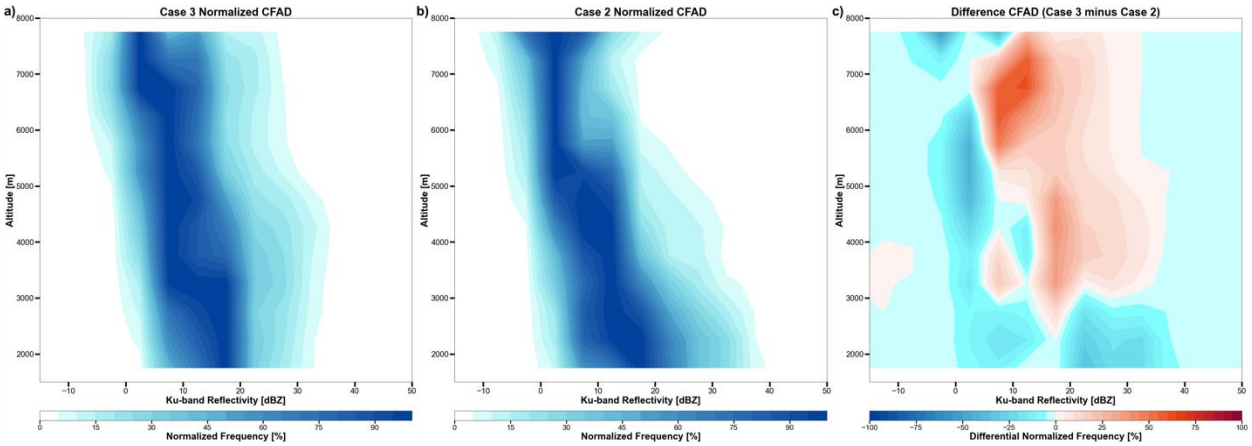

Figure 24: Same as Figure 22, but for Case 3 and Case 2.

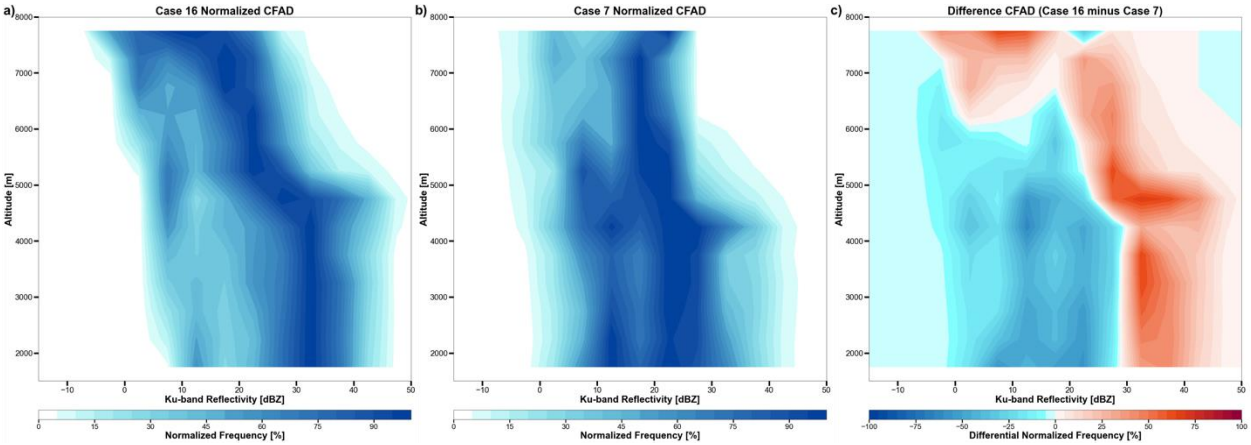

Figure 25: Same as Figure 22, but for Case 16 and Case 7.

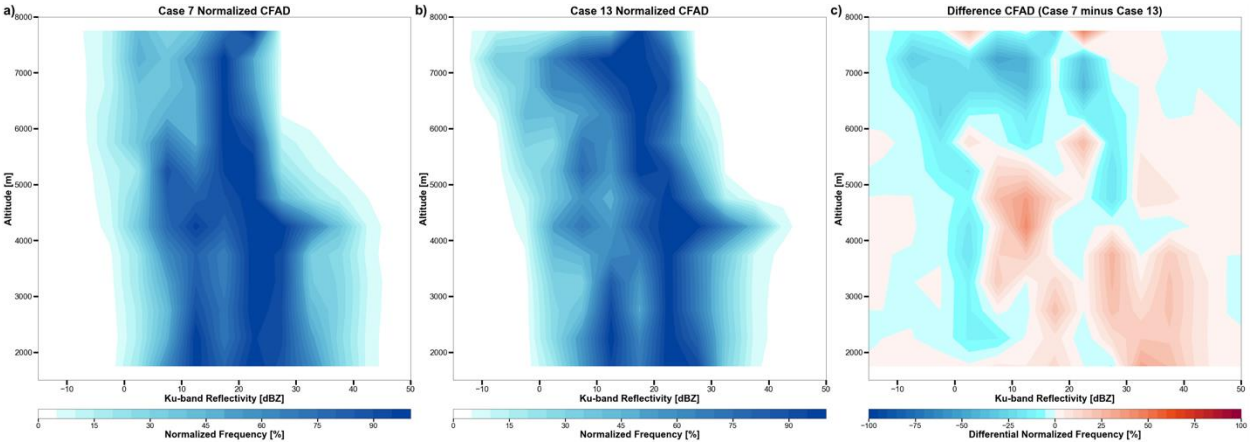

Figure 26: Same as Figure 22, but for Case 7 and Case 13.

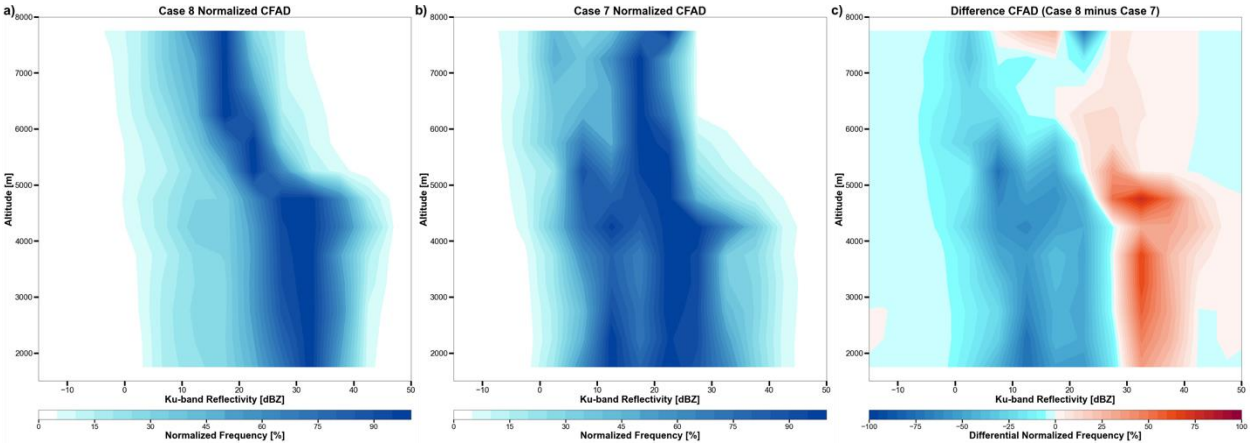

Figure 27: Same as Figure 22, but for Case 8 and Case 7.

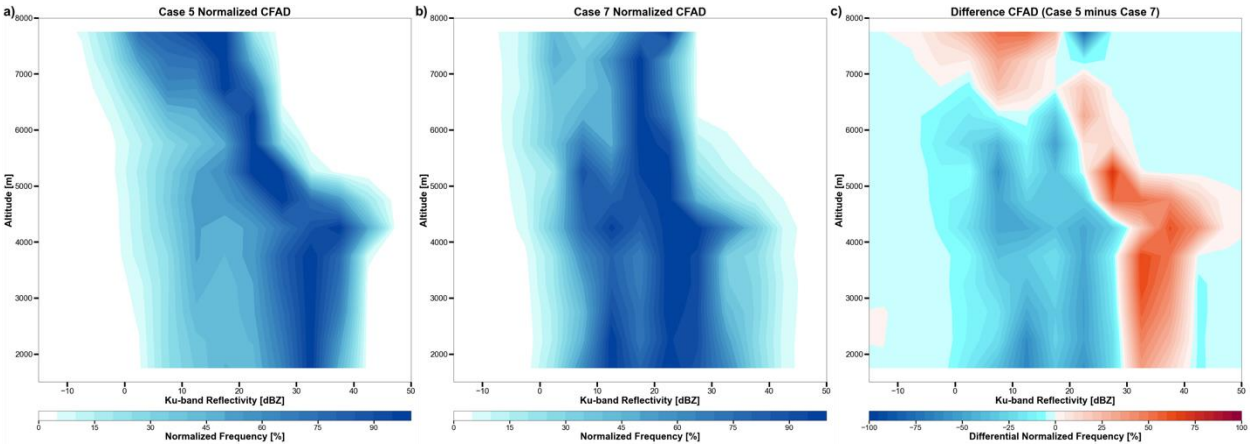

Figure 28: Same as Figure 22, but for Case 5 and Case 7.

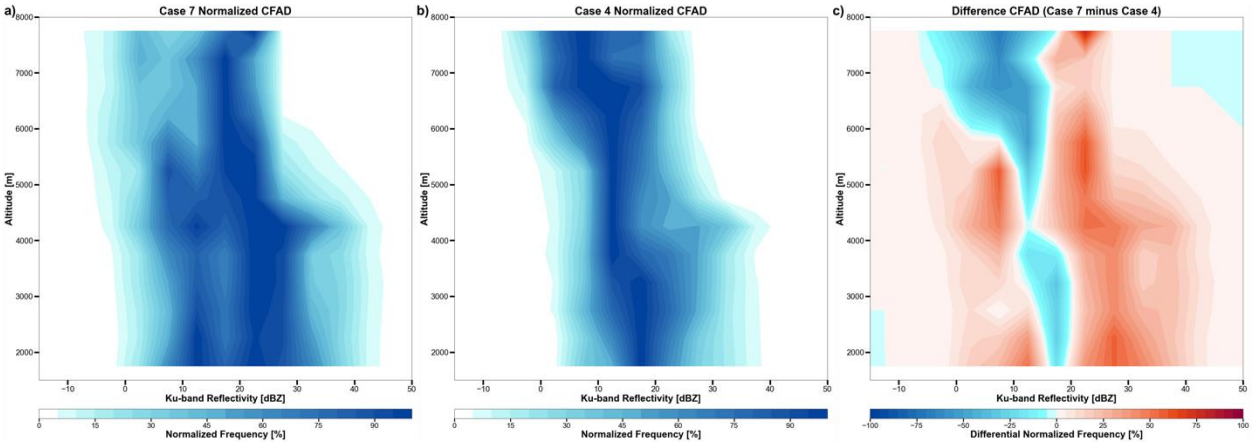

Figure 29: Same as Figure 22, but for Case 7 and Case 4.

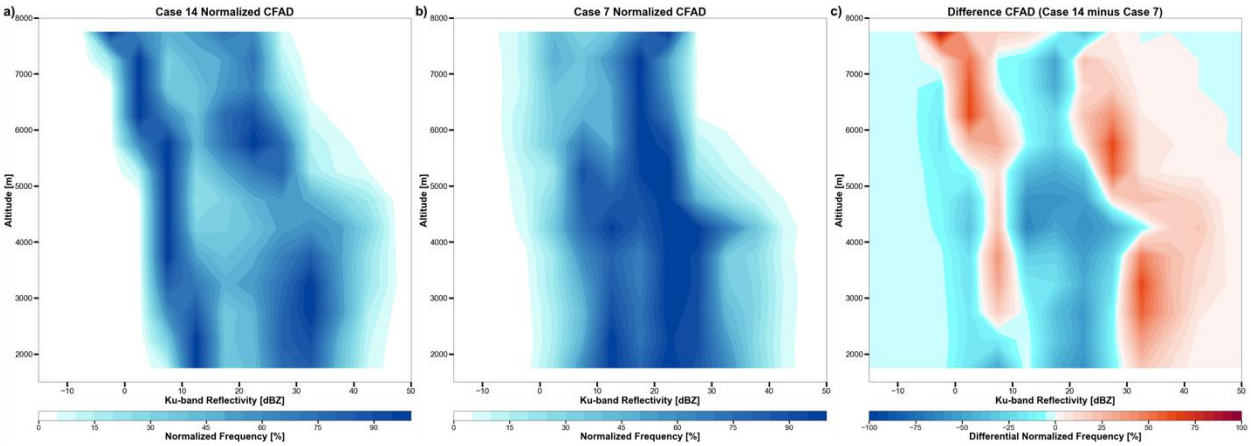

Figure 30: Same as Figure 22, but for Case 14 and Case 7.

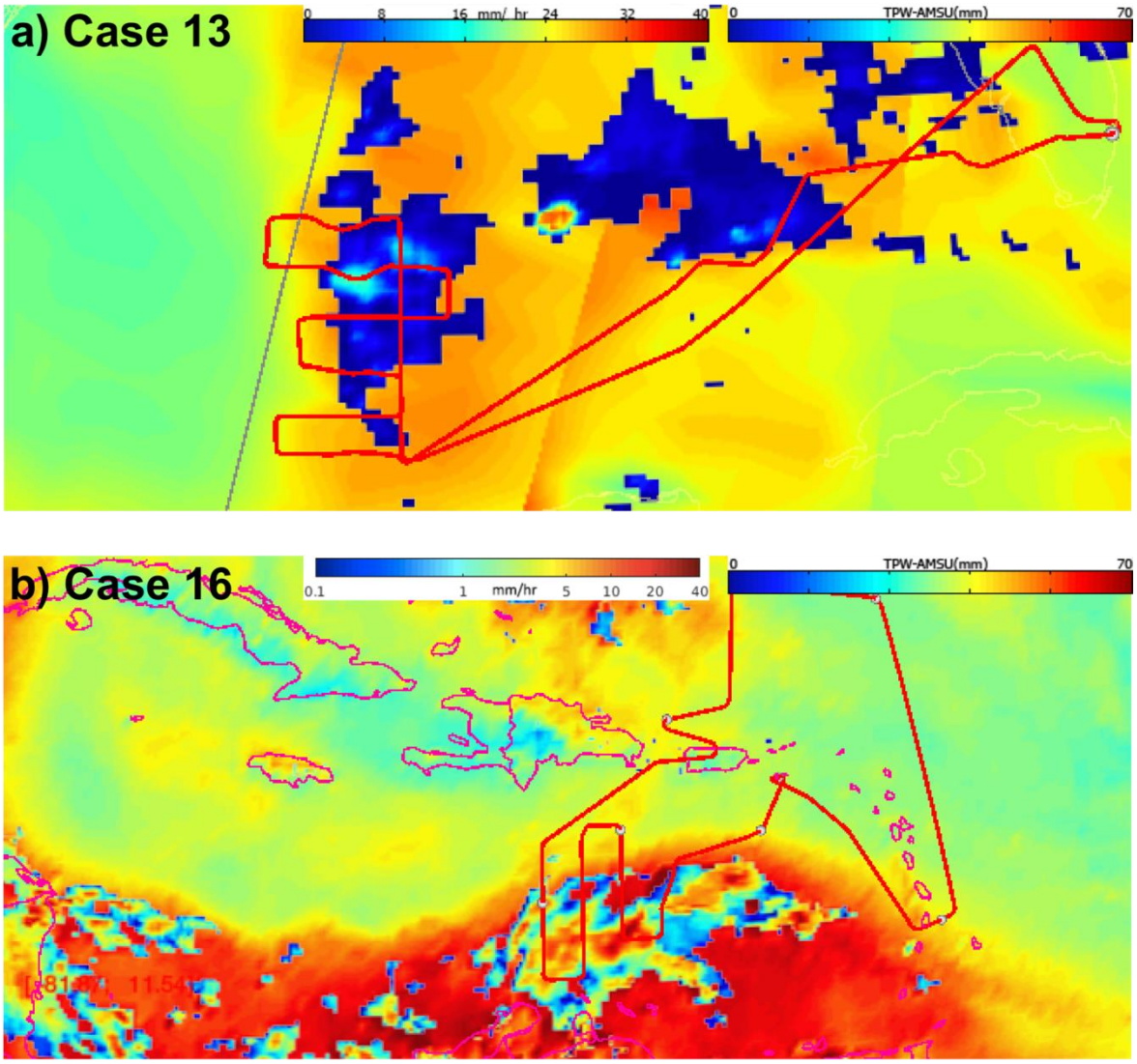

Figure 31: (a) Case 13 TPW (bottom layer fill), GPM IMERG surface precipitation estimation (top layer fill), and DC-8 science flight track (red line). (b) Same as (a), but for Case 16.

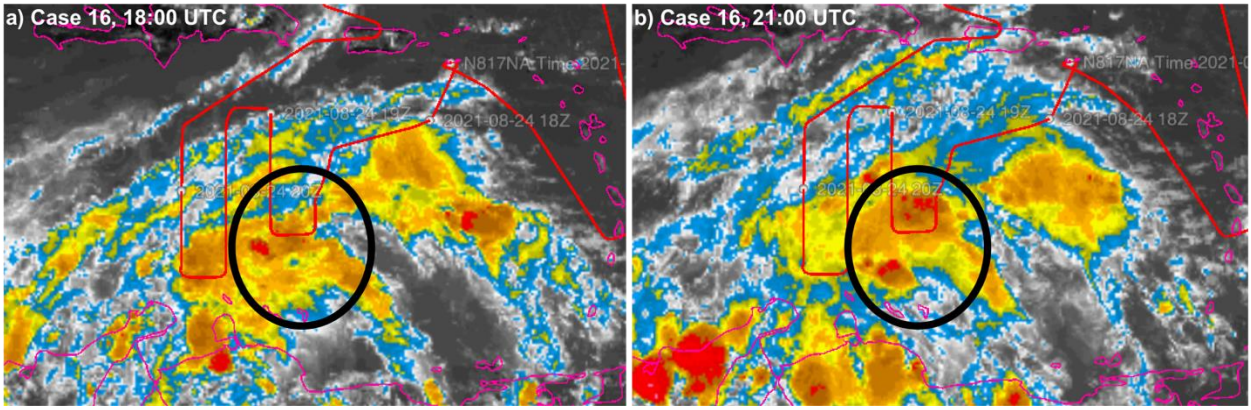

Figure 32: (a) Case 16 GOES-16 IR COLOR at 18:00 UTC (intensifying sector circled in black) and DC-8 science flight track (red line). (b) Same as (a), but at 21:00 UTC.

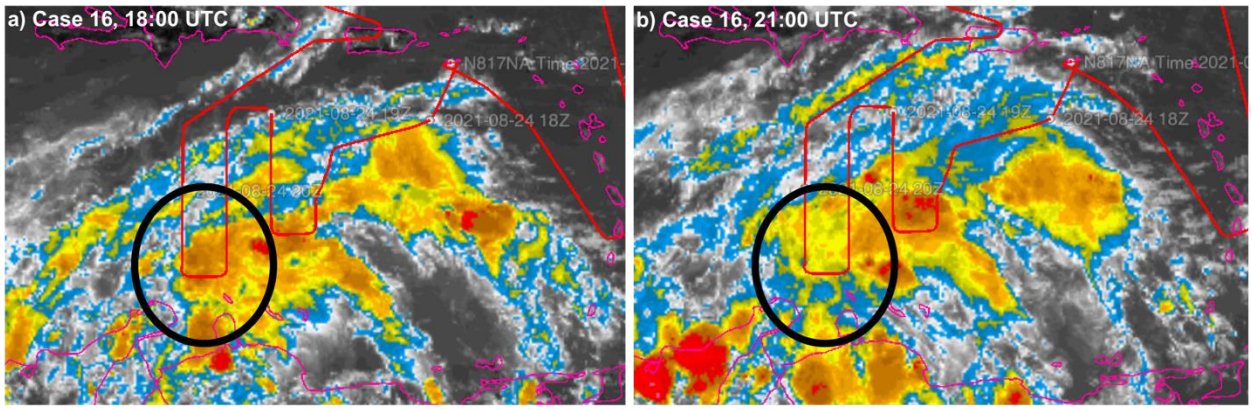

Figure 33: Same as Figure 32, except the matured sector is circled in black.

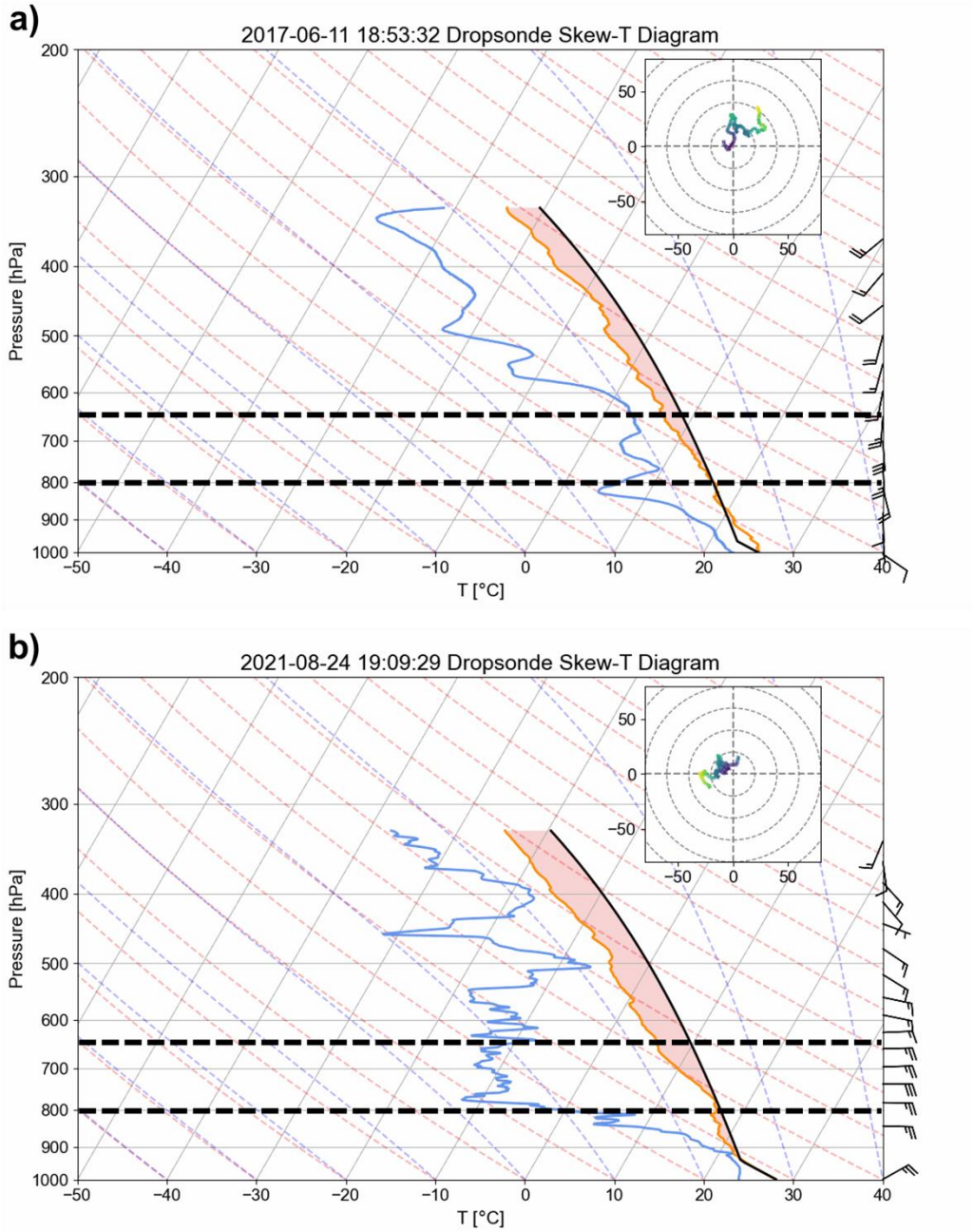

Figure 34: Dropsonde skew-T diagram and hodograph showing the presence of an 800 – 650 mb mid-level jet (wind barbs within black dashed lines) at (a) 18:53:32 UTC from Case 13 and (b) 19:09:29 UTC from Case 16. CAPE is shaded in light red, full lines on wind barbs represent 5 m s^{-1}, and half lines on wind barbs represent 2.5 m s^{-1}.

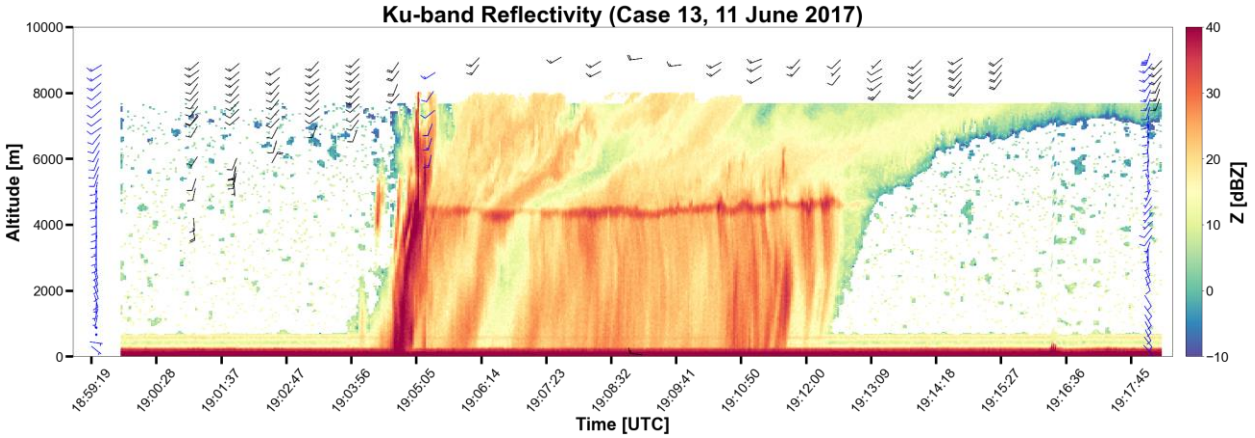

Figure 35: APR-3 Ku-band reflectivity profiles (fill), dropsonde wind profiles (blue barbs), and DAWN wind profiles (black barbs) for Case 13, showing Case 13 to have a leading line, trailing stratiform vertical organizational structure.

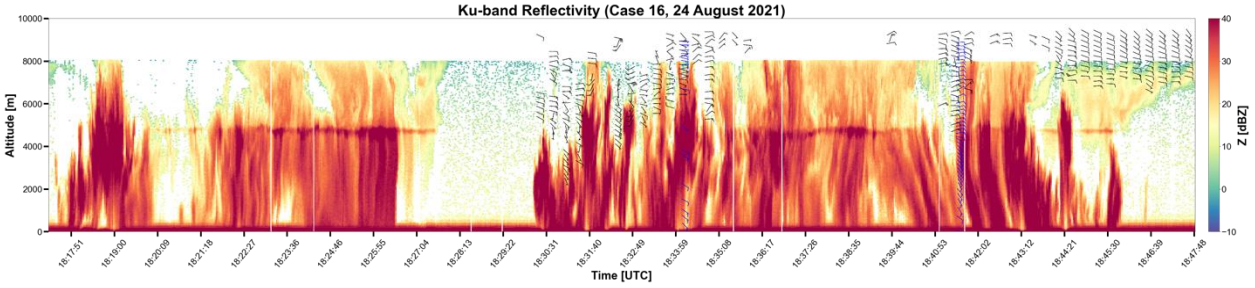

Figure 36: Same as Figure 35, but for Case 16, showing Case 16 to have a vertical organizational structure with many embedded convective elements amongst prevailing stratiform.

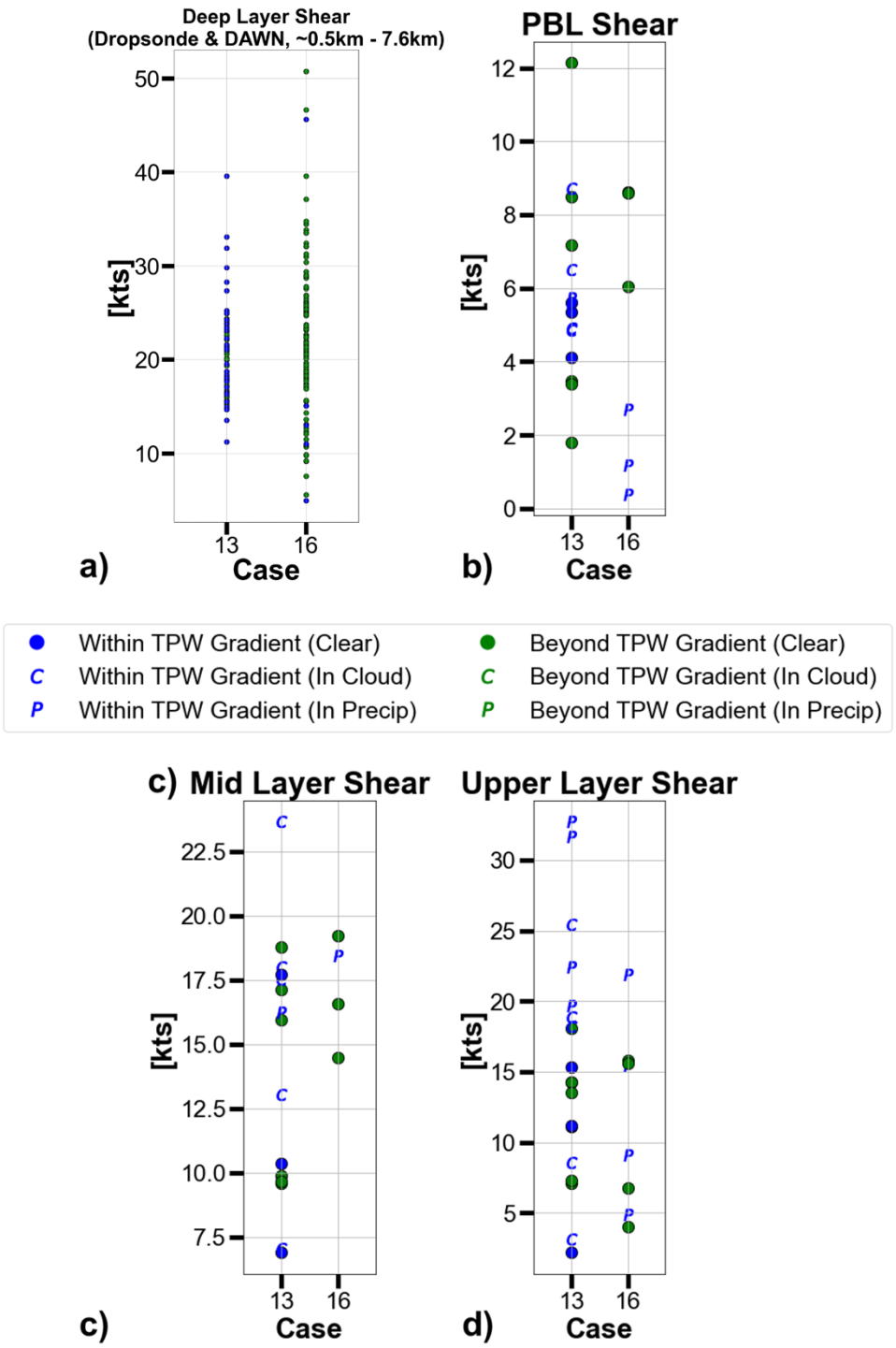

Figure 37: Dropsonde-derived (a) 0.5-km – 7.6-km deep layer speed shear (DAWN observations included as well), (b) PBL speed shear, (c) mid layer speed shear, and (d) upper layer speed shear for Case 13 and Case 16. Observations are color-coded by the location of their dropsondes relative to the synoptic-scale moisture gradient, and their markers denote the convective-relative environments their dropsondes were deployed into.

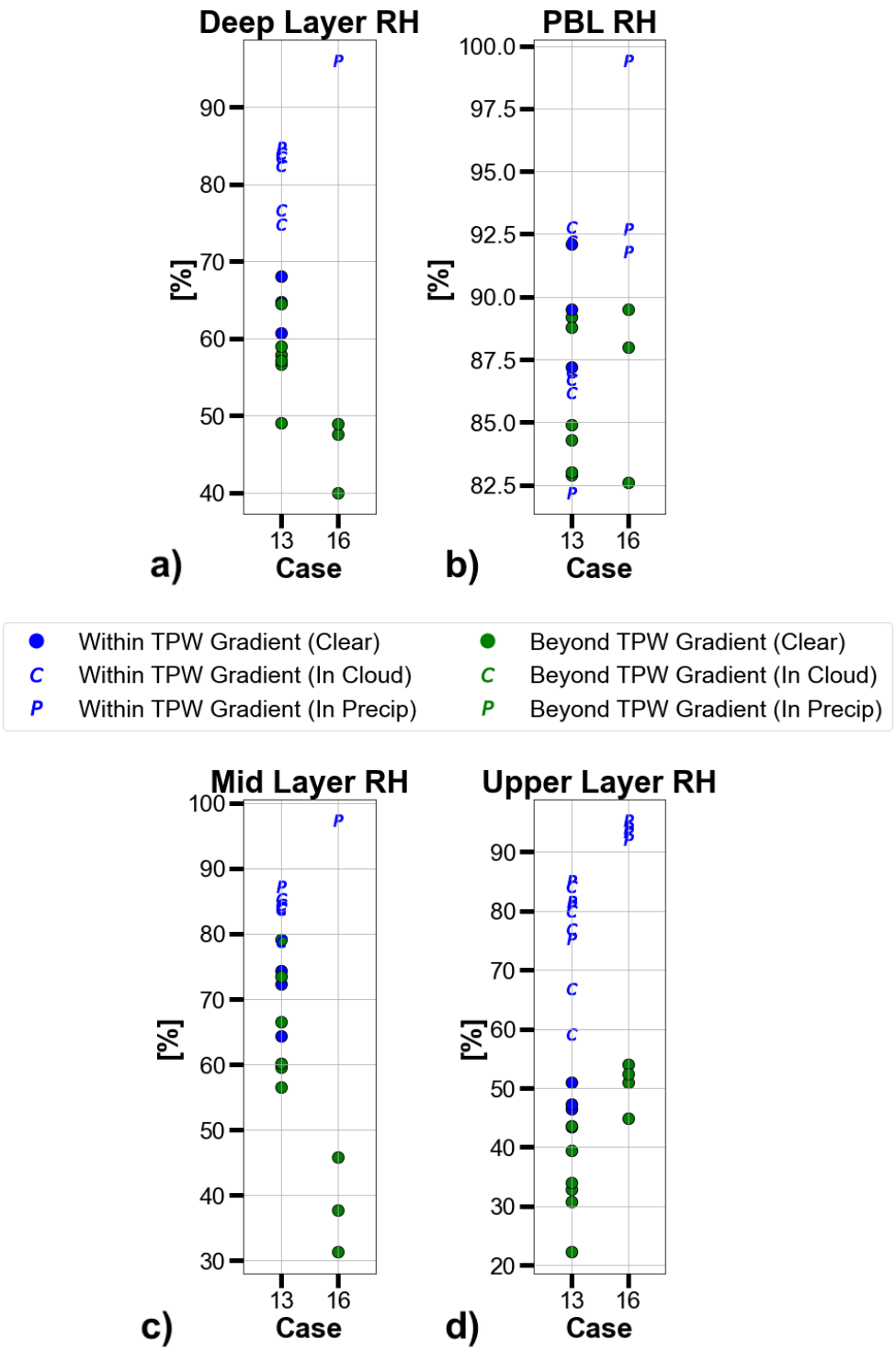

Figure 38: Same as Figure 37, excepting showing (a) deep layer RH, (b) PBL RH, (c) mid layer RH, and (d) upper layer RH.

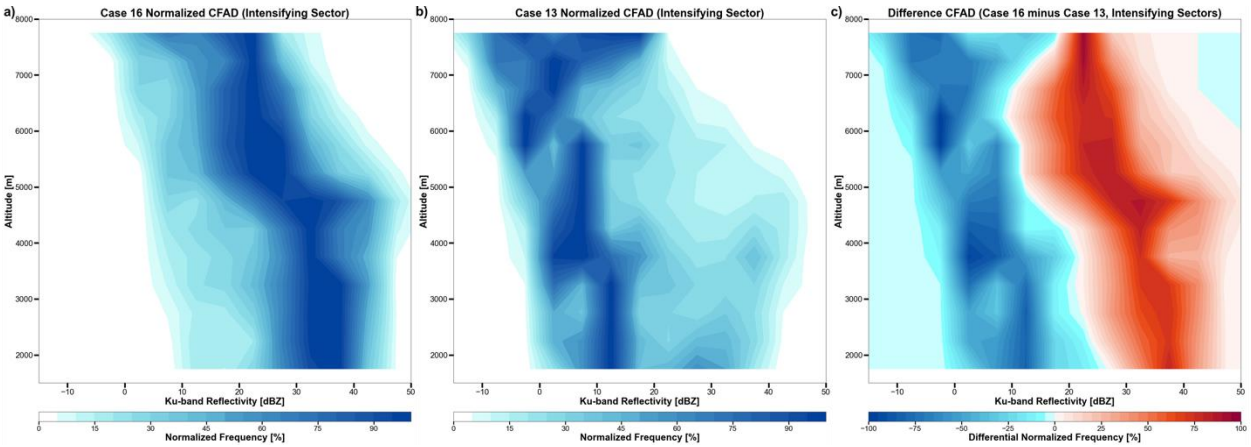

Figure 39: Same as Figure 22, but for the intensifying sectors of Case 16 and Case 13.

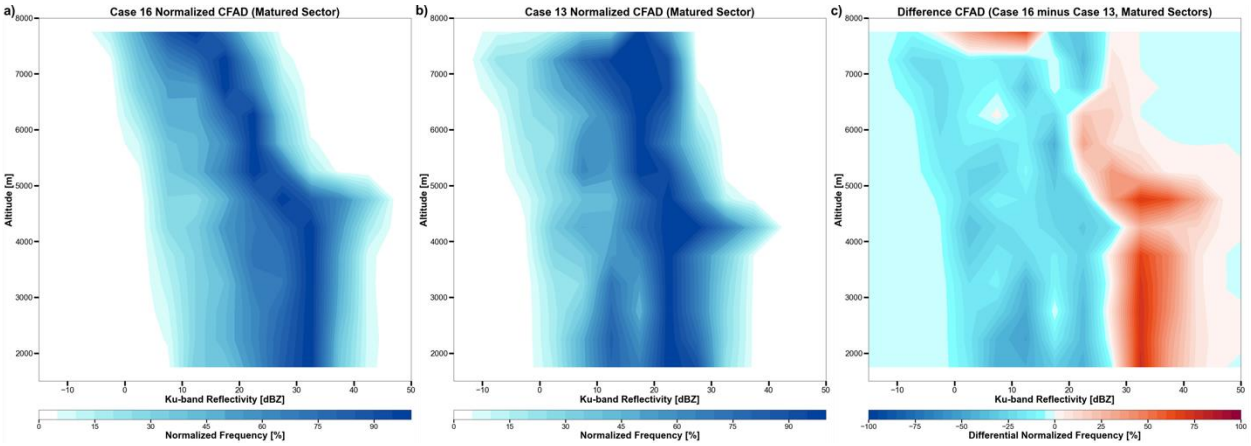

Figure 40: Same as Figure 22, but for the matured sectors of Case 16 and Case 13.

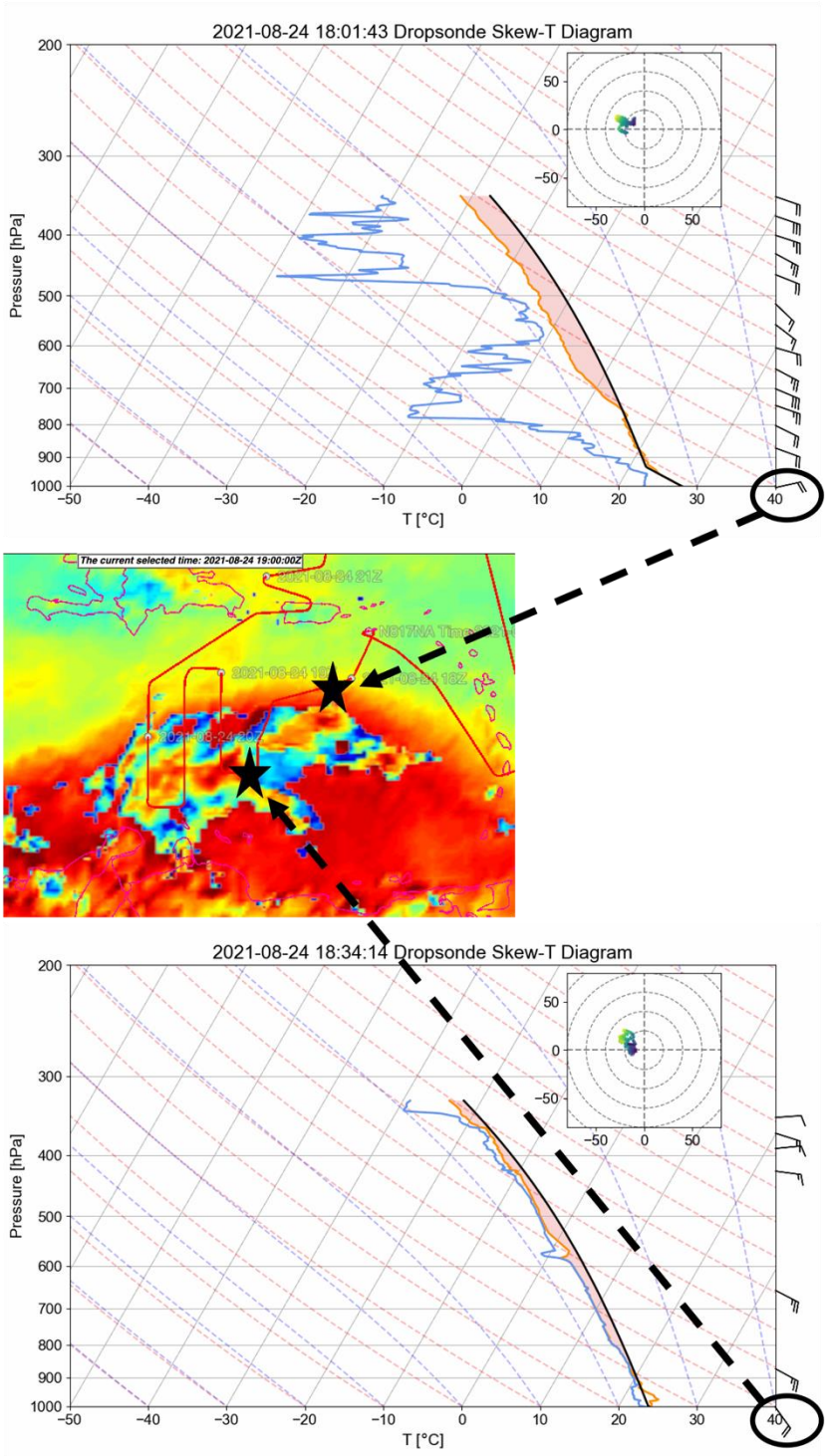

Figure 41: (bottom) Dropsonde skew-T diagram and hodograph (18:34:14 UTC) from the southern half of Case 16 (center) showing near-surface southeasterly winds (black oval). (top) Dropsonde skew-T diagram and hodograph (18:01:43 UTC) from the northern half of Case 16 (center) showing near-surface northeasterly winds (black oval). For each dropsonde skew-T diagram, CAPE is shaded in light red, full lines on wind barbs represent 5 m s^{-1}, and half lines on wind barbs represent 2.5 m s^{-1}.

Chapter 5

Discussion

a) Near-storm Environmental Relationships with Convective Type

The analysis presented in Section 4a investigated near-storm environmental relationships with 2-D TOC structure in the CPEX(-AW) observational domain. While each mean-layer near-storm environmental metric varied widely within a given convective type, notable environmental trends with convective type emerged amongst the variability. Median PBL depth was similar for both isolated and organized TOC (Figure 11a). However, organized TOC was associated with deeper lower and upper quartile PBL depth (Figure 11a), potentially implying stronger cold pool presence that would more significantly alter pre-existing PBL characteristics (e.g., depth). With this assumption, the PBL depth results of this study regionally differ from DYNAMO studies in the Indian Ocean, wherein stronger cold pools (and subsequently longer PBL recovery times, a proxy for PBL depth) were generally associated with more isolated convection (Savarin et al., 2014; Chen et al., 2016; Chandra et al., 2018). However, Chandra et al. (2018) acknowledges the two strongest cold pools in their DYNAMO study were associated with more organized convection. Despite apparent regional differences in PBL depth relationships with convective type, the CPEX(-AW) observations link PBL depth with mid-level dryness ($R_{Pearson} \approx 0.537$, Figure 42). This result is consistent with the DYNAMO studies that relate drier mid-levels (via enhanced dry air entrainment promoting stronger cold pools) to longer PBL recovery times, and it further highlights

the importance of mid layer moisture on near-storm PBL modification (Savarin et al., 2014; Chen et al., 2016; Chandra et al., 2018).

Median MUCAPE and MLCAPE in each layer was found to be slightly greater for isolated TOC (Figure 12), though large CAPE variability between cases of similar convective type ultimately led to no clear CAPE trends with convective type. The unclear CAPE trends are consistent with Lucas et al. (1994), which argues no correlation between CAPE and TOC structure due to more uniform tropical oceanic CAPE distributions compared to other environmental metrics. However, like many prior observational studies of CAPE and TOC (e.g., Chudler and Rutledge, 2021), CPEX(-AW) likely sampled near-storm environments where CAPE was both unrealized and separately already realized. Combining unrealized and realized CAPE observations, which could not be distinguished, in the analysis could partly explain the lack of consistent CAPE relationships with convective type seen in this study.

Investigations of near-storm, mean-layer RH revealed deep layer RH to be generally lesser for organized TOC (Figure 14a, Figure 15a) and PBL RH to be generally greater for organized TOC (Figure 14b, Figure 15b). The deep layer RH result was unexpected and conflicts with the prevailing idea that a drier tropical troposphere inhibits TOC development through enhanced dry air entrainment and negative buoyancy introduction. The PBL RH result was expected and is consistent with CRM (Tompkins, 2001) and ERA-Interim reanalysis (Chen et al., 2017) studies, yet conflicts with KWAJEX observations in the west Pacific (Cetrone and Houze, 2006). Mid and upper layer RH relationships with convective type were unclear (Figure 15c,d), which was also unexpected and regionally differs from observational studies in the west Pacific (e.g., Brown and

Zhang, 1997; LeMone et al., 1998; Cetrone and Houze, 2006). The observed mean-layer RH relationships of this study could be inconsistent with other studies due to legitimate regional variation, but also incorporation of observations from different convective regions and lifecycle stages (e.g., Mechem et al., 2002; see Section 1).

Organized convection was hypothesized to be associated with greater vertical speed shear in each of the four analyzed layers. The hypothesis was validated for the PBL and mid layer (Figure 16b,c), with the PBL findings consistent with prior ERA-Interim reanalysis and PISTON observational studies (e.g., Chen et al., 2017 and Chudler and Rutledge, 2021), along with prevailing cold pool convective initiation theory (Yuter and Houze, 1995; Houze, 2018). Unclear relationships between convective type and both deep (Figure 18c) and upper layer (Figure 17d) speed shear existed, which was unexpected. In particular, the lack of deep layer speed shear trend with convective type differs from CRM, ERA-Interim reanalysis, and TOGA COARE studies that link stronger deep layer shear to more organized TOC (Tompkins, 2001; Igel and van den Heever, 2015; Saxen and Rutledge, 2000). These prior deep layer shear studies were predominately based on observations of quasi-linear TOC, however, and thus may not be directly comparable to the CPEX(-AW) observations that sampled few quasi-linear convective systems.

b) Near-storm Environmental Relationships with Convective Intensity

Motivated by large near-storm environmental metric variability within convective type and between cases of similar convective type, analysis of TOC vertical structure (i.e., convective intensity) found stronger isolated TOC to only be consistently associated with greater mean-layer MLCAPE. This result was consistent for both the median Ku-band reflectivity profile analysis in

Section 4b (Figure 19e,g) and the CFAD analysis in Section 4c (Figure 13b,d; Figure 22c; Figure 23c). The relationship between isolated convective intensity and MLCAPE is in-line with observations from TOGA COARE (Kingsmill and Houze, 1999) and the concept of greater CAPE promoting hydrometeor growth through enhanced thermodynamic instability and buoyancy. The CPEX(-AW) results differ from KWAJEX (Cetrone and Houze, 2006) and PISTON (Chudler and Rutledge, 2021) observations, however, but the contrast could be attributed to negatively biased KWAJEX and PISTON CAPE measurements (see Section 1).

Meanwhile, no clear mean-layer CAPE nor speed shear relationships with organized TOC intensity were observed. However, cases with distinctly greater clear air upper layer RH were consistently more intense than their counterparts (Figure 15d; Figure 27c; Figure 30c), similar to KWAJEX observations in the west Pacific (Cetrone and Houze, 2006). The result is consistent with the theory of less dry air entrainment encouraging intensification through limiting negative buoyancy introduction into the convective system and enabling greater hydrometeor growth. However, this logic was expected to translate to moisture in other layers as well, which was not observed.

In comparison, a lack of similar trends between environmental metrics and convective intensity across convective type indicates that single-core and multi-core systems interact differently with their near-storm environments. As such, further observational investigation into distinguishing process-level features of single-core and multi-core TOC is needed to better understand and forecast TOC.

c) Synoptic-scale Low-level Convergence and Differing Vertical Structures of Organized TOC

Motivated by notably different vertical organizational structures despite similar 2-D structures and synoptic-scale setups, two organized TOC cases were analyzed against one another to determine potential links between multi-core TOC vertical structure and near-storm environments. The case with numerous embedded convective elements amongst prevailing stratiform (i.e., Case 16; Figure 36) was associated with similar speed shear and a distinctly drier impinging synoptic airmass compared to the leading line, trailing stratiform case (i.e., Case 13; Figure 35). Despite notably drier impinging air, Case 16 was more intense than Case 13 (Figure 39c; Figure 40c). This result was unexpected, based on prior observational (Brown and Zhang, 1997; LeMone et al., 1998; Cetrone and Houze, 2006), CRM (Tompkins, 2001), and ERA-Interim (Chen et al., 2017) studies that consistently link more intense TOC to greater mid-level RH via less dry air entrainment. However, cases 13 and 16 were both located on the moist side of their respective synoptic-scale moisture gradient (Figure 31). With Case 16 lacking quality RH observations within the moisture gradient, moisture observations could not be compared from the environments where both cases directly flourished. Therefore, evaluating the Case 13 vs. Case 16 RH analysis in the context of other studies may not be an apt comparison. Upon further investigation, synoptic-scale low-level convergence appeared to be the key force in driving the greater intensity of Case 16 (Figure 41) and perhaps even the greater number of convective elements. Therefore, future observational investigation of synoptic-scale low-level convergence in relation to multi-core organizational structure and TOC intensity is warranted.

d) Caveats

The analysis and results of this study are valuable in addressing the regional gap in *in situ* research of non-tropical cyclone related TOC in the CPEX(-AW) observational domain. That being said, limitations exist with the data, as is inherently the case with field campaigns. The presented analysis is based on observations from a small sample size of 12 convective cases (4 isolated, 8 organized), and many dropsondes were omitted from analysis due to dysfunctionality (e.g., moisture biases). Additionally, the CPEX(-AW) science flights did not consistently sample convection in a similar region relative to the convection, so observations are often being compared from different regions of storms. Contextualizing observations by storm-relative region was attempted, but further dividing the already limited number of observations provided too small of sample sizes for noteworthy comparison. Given the regional variability of near-storm environmental relationships with TOC (e.g., Chen et al., 2017 and as previously discussed in this section), the results of this paper are also specific to the Gulf of Mexico, Caribbean Sea, and western Atlantic region and cannot be confidently translated to other tropical oceanic regions.

e) Figures

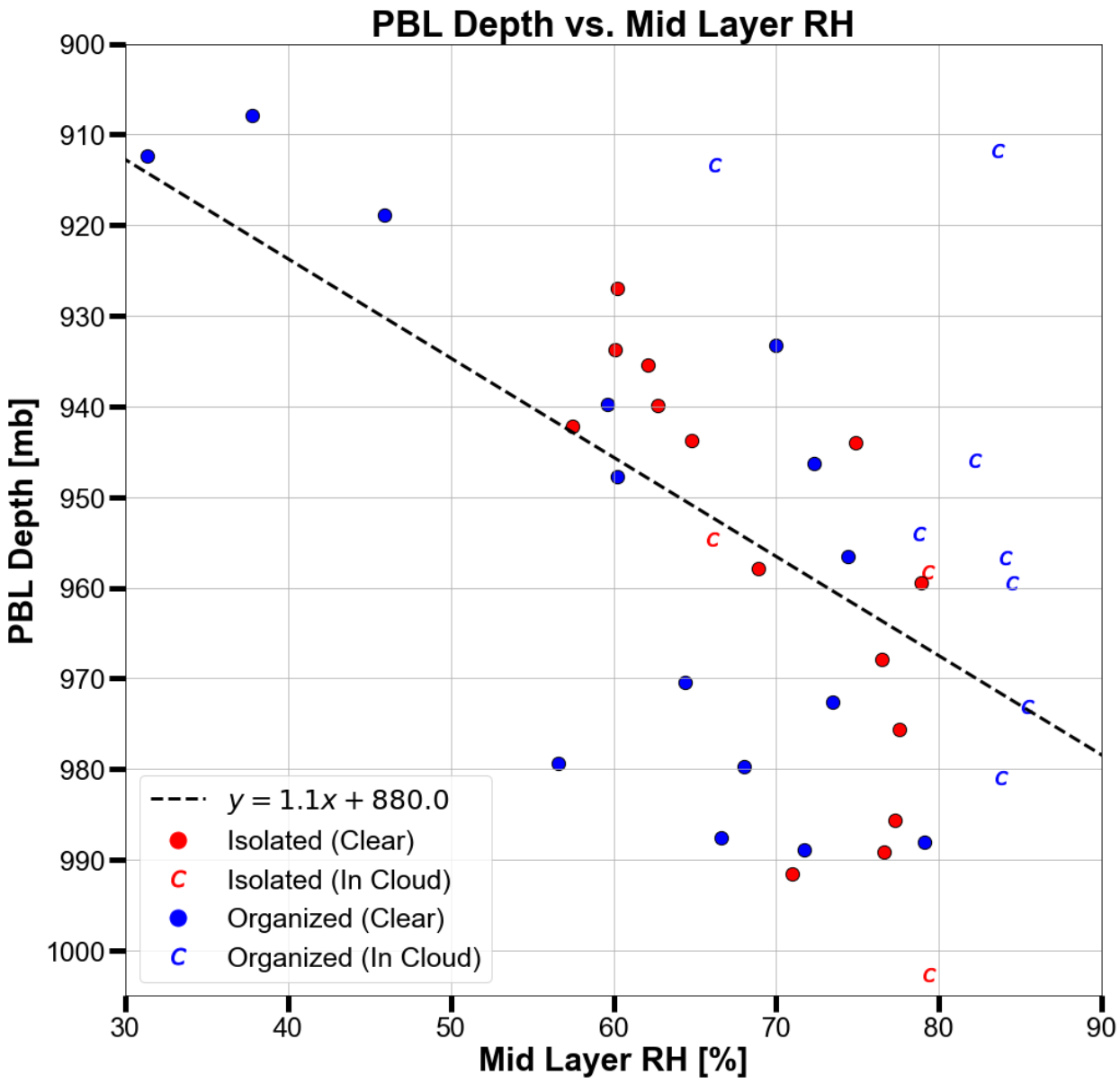

Figure 42: Dropsonde-derived PBL depth vs. mean mid layer RH (In Precip dropsondes excluded). Observations are color-coded by the convective type of the case they were associated with, and their markers denote the convective-relative environments their dropsondes were deployed into. A linear regression of the data is overlaid (black dashed line), with a corresponding regression coefficient of 1.1 mb %$^{-1}$ and a Pearson correlation coefficient of 0.537.

Chapter 6

Summary and Conclusions

Using a unique suite of collocated, high-resolution airborne observations of non-tropical cyclone related TOC from the NASA 2017 CPEX and 2021 CPEX-AW field campaigns, this study presented an analysis of near-storm environmental relationships with 3-D TOC structure in the Gulf of Mexico, Caribbean Sea, and western Atlantic region. Large variability in near-storm mean-layer CAPE, vertical speed shear, and RH was observed amongst systems of similar convective type (isolated, organized) and also within individual convective systems. The unexpectedly large environmental metric ranges within each case necessitates future investigation into how near-storm environments coevolve with convection and why they vary considerably, taking into account convective lifecycle stage at the times of sampling.

Despite the large variabilities, notable trends emerged between near-storm environmental metrics and 3-D convective structure. The PBL was the layer most commonly related to 2-D TOC structure, with organized (i.e., multi-core) TOC being associated with generally greater PBL RH and speed shear compared to isolated (i.e., single-core) TOC. While prior studies, combined with this study, find inconsistent relationships between near-storm PBL environments and TOC, a majority of studies, including this study, denote the importance of the PBL and its environmental characteristics to the organization of TOC (e.g., PBL shear influencing TOC linearity, greater PBL RH providing greater convective buoyancy potential, lesser PBL RH providing enhanced low-

level thermodynamic instability). Therefore, accurate PBL representation in weather and climate models is critical to improve TOC parameterization.

Meanwhile, the upper layer (i.e., above the freezing level) was the layer most consistently related to vertical convective structure (i.e., TOC intensity), with more intense isolated TOC being associated with greater upper layer CAPE and more intense organized TOC being associated with greater upper layer RH. A lack of similar environmental trends with TOC intensity across convective type suggests that single-core and multi-core TOC systems interact differently with their near-storm environments, thus necessitating distinguished process-level research on both types of TOC. Additionally, prior studies tend to not discuss upper layer environmental influences on TOC. The results of this study contend that relationships between TOC intensity and environments above the freezing level should be given more attention.

Lastly, a comparison analysis of two horizontally similar multi-core TOC systems with notably different vertical structures denotes the importance of synoptic-scale low-level convergence and its ability to foster intense TOC in otherwise seemingly less favorable near-storm environmental conditions. The analysis also postulates that synoptic-scale low-level convergence may influence the vertical organizational structure of multi-core TOC (e.g., by increasing the number and intensity of convective elements), though more research is needed.

With prior studies (e.g., Chen et al., 2017) showing TOC relationships with near-storm environments to vary regionally, this study helps address a notable regional gap in *in situ* analysis of relationships between TOC structure and near-storm environmental metrics. It also highlights

the unique capabilities of the CPEX(-AW) remote sensing instrumentation in their ability to capture essential small-scale (both spatially and temporally) near-storm environmental features and variability. The CPEX(-AW) instrumentation, particularly DAWN, offer a glimpse into the potential of future spaceborne remote sensing, with higher resolution measurements capable of improving modeling efforts through improved process-level knowledge of tropical convection (e.g., Turk et al., 2020; Mazza and Chen, 2021), data assimilation (e.g., Cui et al., 2020; Hristova-Veleva et al., 2021; Minamide and Posselt, 2022), and model evaluation (e.g., Cui et al., 2020; Minamide and Posselt, 2022).

Future work will extend analysis of near-storm environmental relationships with 3-D TOC structure to the east Atlantic region using *in situ* observations from the recent 2022 NASA CPEX-Cabo Verde (CPEX-CV) field campaign. CPEX-CV sampled TOC with similar instrumentation to that of CPEX-AW. Unlike CPEX-AW, however, CPEX-CV science flights included a focus on repeated sampling of the same convective systems, providing the opportunity to better analyze and compare specific TOC regions that could not be adequately performed in this study. Furthermore, idealized TOC simulations using the NCAR Cloud Model 1 will also be executed, wherein input sounding moisture and winds (informed by CPEX(-AW) observations) will be altered to analyze their effects on convective structure and organization. TOC relationships with near-storm environments will be explored from satellite and reanalysis perspectives as well. Using collocated archived GPM-DPR, GOES, Atmospheric Infrared Sounder, and Megha-Tropiques remote sensing data, along with NASA MERRA-2 reanalysis, this analysis will help assess satellite and reanalysis capabilities to resolve fundamental TOC features and environmental relationships. In addition to the environmental metrics discussed in this paper, near-storm low-level convergence

and moist static energy will be assessed in relation to TOC structure, as they have both been shown to influence TOC. Ultimately, future work will supplement the *in situ* analysis of this paper, provide an interregional analysis of TOC relationships with near-storm environments, and offer an intercomparison of results across data type (i.e., *in situ* vs. model vs. remote sensing vs. reanalysis).

Bibliography

Alexander, G. D., and G. S. Young, 1992: The relationship between EMEX mesoscale precipitation feature properties and their environmental characteristics. *Monthly Weather Review*, **120**, 554–564, doi:10.1175/1520-0493(1992)120<0554:trbemp>2.0.co;2.

AVAPS Dropsondes. *AVAPS Dropsondes | Earth Observing Laboratory.* https://www.eol.ucar.edu/content/avaps-dropsondes (Accessed May 8, 2023).

Bedka, K. M., and Coauthors, 2021: Airborne lidar observations of wind, water vapor, and aerosol profiles during the NASA Aeolus calibration and validation (Cal/Val) test flight campaign. *Atmospheric Measurement Techniques*, **14**, 4305–4334, doi:10.5194/amt-14-4305-2021.

Black, P., L. Harrison, M. Beaubien, R. Bluth, R. Woods, A. Penny, R. W. Smith, and J. D. Doyle, 2017: High-definition sounding system (HDSS) for atmospheric profiling. *Journal of Atmospheric and Oceanic Technology*, **34**, 777–796, doi:10.1175/jtech-d-14-00210.1.

Blumberg, W. G., K. T. Halbert, T. A. Supinie, P. T. Marsh, R. L. Thompson, and J. A. Hart, 2017: SHARPpy: An open-source sounding analysis toolkit for the atmospheric sciences. *Bulletin of the American Meteorological Society*, **98**, 1625–1636, doi:10.1175/bams-d-15-00309.1.

Brown, R. G., and C. Zhang, 1997: Variability of midtropospheric moisture and its effect on cloud-top height distribution during TOGA COARE*. *Journal of the Atmospheric Sciences*, **54**, 2760–2774, doi:10.1175/1520-0469(1997)054<2760:vommai>2.0.co;2.

Cetrone, J., and R. A. Houze, Jr., 2006: Characteristics of tropical convection over the ocean near Kwajalein. *Monthly Weather Review*, **134**, 834–853, doi:10.1175/mwr3075.1.

Chandra, A. S., P. Zuidema, S. Krueger, A. Kochanski, S. P. Szoeke, and J. Zhang, 2018: Moisture distributions in tropical cold pools from equatorial Indian Ocean observations and cloud-resolving simulations. *Journal of Geophysical Research: Atmospheres*, **123**, doi:10.1029/2018jd028634.

Chen, B., C. Liu, and B. E. Mapes, 2017: Relationships between large precipitating systems and atmospheric factors at a grid scale. *Journal of the Atmospheric Sciences*, **74**, 531–552, doi:10.1175/jas-d-16-0049.1.

Chen, S. S., and Coauthors, 2016: Aircraft observations of dry air, the ITCZ, convective cloud systems, and cold pools in MJO during DYNAMO. *Bulletin of the American Meteorological Society*, **97**, 405–423, doi:10.1175/bams-d-13-00196.1.

Chudler, K., and S. A. Rutledge, 2021: The coupling between convective variability and large-scale flow patterns observed during PISTON 2018-19. *Journal of Climate*, **34**, 7199-7218, doi:10.1175/jcli-d-20-0785.1.

CPEX APR-3, 2018: CPEX APR-3 data read me. National Aeronautics and Space Administration Doc., https://tcis.jpl.nasa.gov/data/cpex/apr3/APR3_CPEX_Format_R2_180425.pdf.

CPEX DAWN, 2019: CPEX DAWN data read me. National Aeronautics and Space Administration Doc., https://tcis.jpl.nasa.gov/data/cpex/dawn/v5/CPEX_DAWN_README.txt.

CPEX Dropsonde, 2019: CPEX dropsonde data read me. National Aeronautics and Space Administration Doc., https://tcis.jpl.nasa.gov/data/cpex/dropsonde/v2_2019-03/CPEX_DROPSONDE_README.txt03/CPEX_DROPSONDE_README.txt.

Cui, Z., Z. Pu, G. D. Emmitt, and S. Greco, 2020a: The impact of airborne Doppler Aerosol Wind (DAWN) lidar wind profiles on numerical simulations of tropical convective systems during the NASA Convective Processes Experiment (CPEX). *Journal of Atmospheric and Oceanic Technology*, **37**, 705–722, doi:10.1175/jtech-d-19-0123.1.

Durden, S. L., L. Li, E. Im, and S. H. Yueh, 2003: A surface reference technique for airborne Doppler radar measurements in hurricanes. *Journal of Atmospheric and Oceanic Technology*, **20**, 269–275, doi:10.1175/1520-0426(2003)020<0269:asrtfa>2.0.co;2.

Durden, S. L., S. Tanelli, and E. Im, 2012: Recent observations of clouds and precipitation by the Airborne Precipitation Radar 2nd generation in support of the GPM and ACE Missions. *SPIE Proceedings*, doi:10.1117/12.977574.

Greco, S., G.D. Emmitt, and M. Garstang, 2018: Overview of YES dropsonde performance during CPEX and YES QC. CPEX Science Team Workshop, Salt Lake City, UT [Available online at https://cpex.jpl.nasa.gov/cpex2017/scienceteammeeting/2018/SteveGRECO_CPEX_SLC_DROP_FINAL.pdf.]

Greco, S., G. D. Emmitt, M. Garstang, and M. Kavaya, 2020: Doppler Aerosol Wind (DAWN) lidar during CPEX 2017: Instrument performance and data utility. *Remote Sensing*, **12**, 2951, doi:10.3390/rs12182951.

Guy, N., and D. P. Jorgensen, 2014: Kinematic and precipitation characteristics of convective systems observed by airborne Doppler radar during the life cycle of a Madden–Julian Oscillation in the Indian Ocean. *Monthly Weather Review*, **142**, 1385–1402, doi:10.1175/mwr-d-13-00252.1.

Houze, R. A., Jr., 2018: 100 years of research on mesoscale convective systems. *Meteorological Monographs,* **59**, doi:10.1175/amsmonographs-d-18-0001.1.

Houze, R. A., Jr., K. L. Rasmussen, M. D. Zuluaga, and S. R. Brodzik, 2015: The variable nature of convection in the tropics and subtropics: A legacy of 16 years of the Tropical Rainfall Measuring Mission Satellite. *Reviews of Geophysics*, **53**, 994–1021, doi:10.1002/2015rg000488.

Hristova-Veleva, S., S. Q. Zhang, F. J. Turk, Z. S. Haddad, and R. C. Sawaya, 2021: Assimilation of DAWN Doppler wind lidar data during the 2017 Convective Processes Experiment (CPEX): Impact on precipitation and flow structure. *Atmospheric Measurement Techniques*, **14**, 3333–3350, doi:10.5194/amt-14-3333-2021.

Igel, M. R., and S. C. van den Heever, 2015: The relative influence of environmental characteristics on tropical deep convective morphology as observed by CloudSat. *Journal of Geophysical Research: Atmospheres*, **120**, 4304–4322, doi:10.1002/2014jd022690.

Kavaya, M. J., J. Y. Beyon, G. J. Koch, M. Petros, P. J. Petzar, U. N. Singh, B. C. Trieu, and J. Yu, 2014: The Doppler Aerosol Wind (DAWN) airborne, wind-profiling coherent-detection lidar system: Overview and preliminary flight results. *Journal of Atmospheric and Oceanic Technology*, **31**, 826–842, doi:10.1175/jtech-d-12-00274.1.

Kingsmill, D. E., and R. A. Houze, Jr., 1999: Thermodynamic characteristics of air flowing into and out of precipitating convection over the west Pacific warm pool. *Quarterly Journal of the Royal Meteorological Society*, **125**, 1209–1229, doi:10.1002/qj.1999.49712555606.

LeMone, M. A., E. J. Zipser, and S. B. Trier, 1998: The role of environmental shear and thermodynamic conditions in determining the structure and evolution of mesoscale convective systems during TOGA COARE. *Journal of the Atmospheric Sciences*, **55**, 3493–3518, doi:10.1175/1520-0469(1998)055<3493:troesa>2.0.co;2.

Liu, S., and X.-Z. Liang, 2010: Observed diurnal cycle climatology of planetary boundary layer height. *Journal of Climate*, **23**, 5790–5809, doi:10.1175/2010jcli3552.1.

Lucas, C., E. J. Zipser, and M. A. Lemone, 1994: Vertical velocity in oceanic convection off tropical Australia. *Journal of the Atmospheric Sciences*, **51**, 3183–3193, doi:10.1175/1520-0469(1994)051<3183:vvioco>2.0.co;2.

Martin, C. and I. Suhr, 2021. NCAR/EOL Atmospheric Sounding Processing Environment (ASPEN) software. Version 3.4.5. [Available online at: https://www.eol.ucar.edu/content/aspen.] (Accessed November 16, 2022).

Mazza, E., and S. S. Chen, 2021: Subsidence warming in the tropical cyclogenesis of Cindy (2017): CPEX observations and coupled modeling. *Journal of the Atmospheric Sciences*, **78**, 3385–3400, doi:10.1175/jas-d-20-0340.1.

Mechem, D. B., R. A. Houze Jr, and S. S. Chen, 2002: Layer inflow into precipitating convection over the western tropical Pacific. *Quarterly Journal of the Royal Meteorological Society*, **128**, 1997–2030, doi:10.1256/003590002320603502.

Minamide, M., and D. J. Posselt, 2022: Using ensemble data assimilation to explore the environmental controls on the initiation and predictability of moist convection. *Journal of the Atmospheric Sciences*, **79**, 1151–1169, doi:10.1175/jas-d-21-0140.1.

Sadowy, G.A., A. Berkun, W. Chun, E. Im, and S. Durden, 2003: Development of an advanced airborne precipitation radar. *Microwave Journal*, **46**, 84-98.

Savarin, A., S. S. Chen, B. W. Kerns, and D. P. Jorgensen, 2014: Convective cold pool structure and boundary layer recovery time in DYNAMO. 31st Conf. on Hurricanes and Tropical Meteorology, San Diego, CA, *Amer. Meteor. Soc.*, **9B.2**. [Available online at https://ams.confex.com/ams/31Hurr/webprogram/Paper245387.html.]

Saxen, T. R., and S. A. Rutledge, 2000: Surface rainfall–cold cloud fractional coverage relationship in TOGA COARE: A function of vertical wind shear. *Monthly Weather Review*, **128**, 407, doi:10.1175/1520-0493(2000)128<0407:srccfc>2.0.co;2.

Tompkins, A. M., 2001: Organization of tropical convection in low vertical wind shears: The role of water vapor. *Journal of the Atmospheric Sciences*, **58**, 529–545, doi:10.1175/1520-0469(2001)058<0529:ootcil>2.0.co;2.

Touzé-Peiffer, L., R. Vogel, and N. Rochetin, 2021: Detecting cold pools from soundings during EUREC4A. arXiv [preprint], arXiv:2104.09146.

Turk, F. J., S. Hristova-Veleva, S. L. Durden, S. Tanelli, O. Sy, G. D. Emmitt, S. Greco, and S. Q. Zhang, 2020: Joint analysis of convective structure from the APR-2 precipitation radar and the DAWN Doppler wind lidar during the 2017 Convective Processes Experiment (CPEX). *Atmospheric Measurement Techniques*, **13**, 4521–4537, doi:10.5194/amt-13-4521-2020.

Vömel, H., and Coauthors, 2021: High-resolution in situ observations of atmospheric thermodynamics using dropsondes during the Organization of Tropical East Pacific Convection (OTREC) field campaign. *Earth System Science Data*, **13**, 1107–1117, doi:10.5194/essd-13-1107-2021.

Yuter, S. E., and R. A. Houze, Jr., 1995: Three-dimensional kinematic and microphysical evolution of Florida cumulonimbus. Part II: Frequency distributions of vertical velocity, reflectivity, and differential reflectivity. *Monthly Weather Review*, **123**, 1941–1963, doi:10.1175/1520-0493(1995)123<1941:tdkame>2.0.co;2.

Zagrodnik, J. P., L. A. McMurdie, R. A. Houze, Jr., and S. Tanelli, 2019: Vertical structure and microphysical characteristics of frontal systems passing over a three-dimensional coastal mountain range. *Journal of the Atmospheric Sciences*, **76**, 1521–1546, doi:10.1175/jas-d-18-0279.1.